Utrecht University

Master Thesis

Proglacial Lakes Elevate Glacier Surface Velocities in the Himalayan Region

Author:
Jan Bouke Pronk

Project Supervisor:
Dr. ir. Bert Wouters
Daily Supervisor:
Dr. Tobias Bolch

A thesis submitted in fulfillment of the requirements for the degree of Master of Science

in the

Institute for Marine and Atmospheric Research Utrecht
Department of Physics
Faculty of Science

July 2020

Preface

The basis for this thesis originally stemmed from my desire to not spend an entire year behind my computer, but instead take this opportunity to see something of the world. This brought me all the way across to Tibet, accompanied by a British chap, a remarkably tall Chinese expedition leader, an enthusiastic Chinese master student, a team of tough Tibetan locals, a few horses and a boat. It was an memorable experience, and under the peaks of the Himalayas I got introduced with the topic I ended working on together with a research group in St Andrews; the relevance of quickly developing lakes at expense of Himalayan glaciers.

Without the opportunity and trust Tobias Bolch gave me to go on fieldwork I would neither have ended up in Tibet nor in St Andrews, and therefore he deserves my thanks for that. I also want to thank the British chap, Owen King, for keeping me company on the Tibetan Plateau and for he always has been available to help me out. At last, but certainly not least, I want to thank my parents for tolerating my presence during these hard times of pandemic.

Abstract

Himalayan glaciers melt into the Ganges and Brahmaputra river catchments that provide water to over half a billion people. Upstream areas are likely to be affected substantially by climate change, and changes in melt-water supply will locally have tremendous consequences for downstream populations. About 10% of the Himalayan glacier population terminates into pro-glacial lakes and such lake-terminating glaciers are known to be capable of accelerating total mass losses by a well studied phenomena called dynamic thinning. However, evidence for dynamic thinning on Himalayan lake-terminating glaciers is sparse and studies available are only local in nature. Here we present, by employing the Sentinel-2 optical satellites, a 2017-2019 glacier surface velocity dataset covering most of the Central and Eastern Himalayan glaciers larger than 3km^2. We find that centre flow line velocities of lake-terminating glaciers are more than twice as high as land terminating glaciers (18.8 to 8.24 m/year), and show substantially more heterogeneity at the glacier snout. We attribute this large heterogeneity to the varying influence of lakes on glacier dynamics, resulting in differential rates of dynamic thinning and show that about half of the lake-terminating glacier, of which most clean-ice, show an acceleration towards the terminus. Many of these clean-ice lake terminating glaciers are disproportionately large and drain into the highly melt-water dependent Brahmaputra basins. With continued warming new lake development is likely to happen and will further accelerate future ice mass losses; a scenario not currently considered in regional projections.

Keywords— Himalayas, Lake-Terminating Glaciers, Glacier Surface Velocity, Dynamic Thinning, Debris Cover, Sentinel-2

Contents

1 Introduction **1**

2 Objectives **6**

3 Study Area **7**

4 Methodology **10**
4.1 Surface Velocity 10
4.1.1 Sentinel-2 Specifications 10
4.1.2 Image Pair Selection 10
4.1.3 Preprocessing 12
4.1.4 Image matching 12
4.1.5 Postprocessing 13
4.2 Assessing the Precision and Uncertainty of the Velocity Field 14
4.2.1 Precision: Median Absolute Deviation (MAD) 14
4.2.2 Uncertainty: 95% Confidence Interval (CI_{95}) 15
4.3 Surface Elevation Change and Estimation of ELA 15
4.4 Glacier Centre Flow Line Analysis 16
4.5 Glacier Surface Slope 16
4.6 Glacier Group Uncertainty 17

5 Results **18**
5.1 Algorithm Performance and Velocity Uncertainty 19
5.2 Comparison with Previous Studies 20
5.3 Terminus Type Variability in Velocity 21
5.3.1 Velocity Dependence on Orientation and Surface Area 22
5.3.2 Regional Variability 24
5.4 Surface Cover on Glacier-Lake Dynamics 25
5.5 Supraglacial Lakes on Glacier Surface Lowering 30

6 Discussion **32**
6.1 Limitations of our Analysis 32
6.2 Lake-Terminating Heterogeneity and Possible Drivers of Dynamic Thinning 33
6.3 Implications for Future Evolution of Himalayan Glaciers 35

7 Conclusions **36**

Appendices **44**

A Additional Materials Velocity Quality Assessment **44**

B Additional Materials Centre Flow Line Analysis **47**

List of Figures

1 Schematic illustration of first-order calving in response to dynamic thinning. Surface crevasses propagate downward to some depth d in response to the velocity gradient $\partial U_B/\partial x$, which relate to the velocity at the surface. Terminus might be either floating or grounded (after Benn et al. (2007a)). 3

2 Map showing the regional subdivisions (red rectangles) and the associated glacier characteristics (pie charts), including terminus type and surface cover as a fraction of the total sub-regional glaciated area. The size of the pie charts correspond to total size of the sub-regional glaciated area, with largest areal ice cover found in Central West 2 (1404 km^2) and smallest in Central West 1 (920 km^2). Transparent fractions of the pie charts represent the area that is not covered in in study. Transboundary rivers are indicated by blue lines, whereas glacier areas are colored white. Country boundaries are tentative and for orientation only. This figure was generated using Matplotlib, vers. 3.1.2, together with Python, vers. 3.7. 7

3 Regional 2007-2019 velocity fields across the Himalaya, with an illustrative distribution of water bodies (blue polygons, after Wangchuck and Bolch (2020)). Subregion Central 1 is for aesthetic reasons separated into two figures. Country boundaries are tentative and for orientation only. This figure was generated using Matplotlib, vers. 3.1.2, together with Python, vers. 3.7. 18

4 Spatial Median Absolute Deviation for both velocity components at a stable area (MAD_{off}) for a single image pair at East Himalaya. The 0.625m periodic distribution results from choices on the subpixel resolution. The vertical dashed lines define the interquartile range. Note that the velocity components largely overlap. For the location of the stable area see fig. A.1 19

5 Dispersion (MAD_{disp}) (a) and 95% confidence interval (CI_{95}) (b) at glacier areas. (a) The red distribution represents the MAD_{disp} before subtracting $\overline{V}_{off}$ from each image pair, which realized a 56% reduction of the median dispersion, resulting in the grey dispersion distribution. (b) CI_{95} resulting from the estimated distribution of median displacement vector as a function of the number is velocity estimates and MAD_{disp} (eq. 11). 20

6 Median CI_{95} (m/year) for lake-terminating glaciers (blue) and land-terminating glaciers (red) along the normalized glacier centre flow line at the ablation zone, with the terminus positioned at the right end of the figure. The spread among the glacier population is represented by the interquartile range (IQR). The numbers shown at the legend indicate the population size. All centre flow line velocities with CI_{95} >5m/year are eliminated. 21

7 Regional median centre flow line surface velocity (m/year) comparison between Dehecq et al. (2019b) (dashed line), Gardner et al. (2019) (dashed-dotted line) and this study (solid line) of glacier greater than 3km^2 in area. All glaciers are normalized along their ablation length with the terminus positioned at the right end of this figure. 22

8 Median centre flow line surface velocity (m/year) (a) and coverage (%) of the velocity estimates (b). (a) The blue line represents the median of lake-terminating glacier, the red line the median of land-terminating glaciers and the black dashed line the whole glacier population. The spread among the glacier population is represented by the IQR, which is only shown around the lake-terminating and land-terminating median. The numbers at the legend indicate the population size.(b) The coverage is defined by the fraction of glaciers showing an uncertainty below 5m/year at a given position along the centre flow line. 23
9 Boxplot showing the mean velocity contrast between lake-terminating glaciers (blue) and land-terminating glaciers (red) depending on the orientation of the ablation zone (a) and surface area (b). Boxes represent the IQR of the distribution, whereas points that are outside of the 3rd quartile plus 1.5 times the IQR range are plotted explicitly. 24
10 Subregional glacier median centre flow line velocity estimates and their location along the CE Himalaya (red rectangles). Blue lines and red lines represent lake-terminating glaciers and land-terminating glaciers respectively. The spread shows the IQR among the glacier population, with the number of glaciers shown in the legend between the brackets. This figure was generated using Matplotlib, vers. 3.1.2, together with Python, vers. 3.7. 26
11 Glacier median centre flow line velocity (m/year) (a,c,e) and surface elevation change (dh/dt) estimates (after King et al. (2019))(b,d,e) for lake-terminating glaciers (blue) and land-terminating glaciers (red). A further subdivision is made between debris-covered glaciers (c,d) and clean-ice glaciers (e,f). The spread shows the IQR among the glacier population, with the number of glaciers shown in the legend between the brackets. 27
12 Glacier median centre flow line velocity (m/year) (a) and surface elevation change (dh/dt) estimates (after King et al. (2019))(b) for debris-covered lake-terminating glaciers (blue) land-terminating glaciers (red) and glaciers with supraglacial lakes (black). The spread among the glacier population is represented by the IQR. The numbers between brackets at the legend indicate the population size. 31
13 Impression of the distribution of transverse crevasses among the lake-terminating glacier population in the Himalayan region, with the dashed yellow lines indicating the orientation of the crevasses. Glaciers RGI60-15.10994 and RGI60-15.02591 (a,c) are (almost) clean-ice glaciers with a clear crevassed zone, whereas glacier RGI60-15.03743 (b) is covered by a thick mantle of debris, though several transverse crevasses are visible. (d) The Guoluo Glacier (RGI60-15.02591) shows a clear crevassed zone, although seems to have retreated to shallow parts of the lake. 34
A.1 Sentinel-2 image tile with the selected surface area used for image-matching represented by the white mask. 44
A.2 Distribution of all absolute median offsets calculated at stable areas ($\overline{V}_{off}$). Red dashed line represents the 95% percentile. 44
A.3 The MAD_{disp} at subselection at region Central 1. Yellow areas indicate surfaces with MAD_{disp} >10m/year. 45

A.4 Regional median centre flow line surface velocity (m/year) comparison between Dehecq et al. (2019b) (dashed line), Gardner et al. (2019) (dashed-dotted line) and this study (solid line) of glacier greater than 10km^2 in area. 46
B.1 Boxplot showing the mean velocity contrast between lake-terminating glaciers (blue) and land-terminating glaciers (red) depending on the orientation of the ablation zone (a) and surface area (b) for the second half of the ablation zone. Boxes represent the IQR of the distribution, whereas points that are outside of the 3rd quartile plus 1.5 times the IQR range are plotted explicitly. 47
B.2 A rough separation of accelerating (a) and deceleration (b) lake-terminating glaciers. A glacier is regarded as accelerating when the mean velocity U_1 is greater than mean velocity U_0. Red dashed line is the estimated location where the acceleration becomes observable. Land-terminating glaciers are plotted for reference. 48

List of Tables

1 Regional distribution of lakes-terminating glaciers and debris-covered glaciers. The numbers without units represent the number of glaciers withing a specific glacier category, with the percentages showing the relative fraction of surface area the subselection occupies within the subregion. The area column shows the area that glaciers of our selection occupy in each subregion, and the coverage being the percentage of the total glacier areal occupation of our glacier selection. The coverage over the whole region (41%) is relatively low since it also incorporates all CE Himalayan glaciers outside our subregions. 8
2 An overview off all the November Sentinel-2 number of images, image pairs and effective date between 2016-2019 for every image tile used in this study. 11
3 Parameters used for image matching and postprocessing. Image matching parameters are given in Sentinel-2 pixel resolution units (10m), whereas postprocessing parameters are given in velocity pixelsize units (80m). *Unitless parameters, see Section 4.1.5 for context. 14
4 Several key characteristics for lake-terminating, land-terminating and all glaciers of this study. Upper and lower bounds represent one standard error (SE). 23
5 Mean of median regional centre flow line velocities of lake-terminating, land-terminating and all glaciers. Uncertainty estimates represent the 1 SE confidence interval. 25
6 Mean of median centre flow line velocities of lake-terminating, land-terminating and all glaciers, subdivided by surface cover. Uncertainty estimates represent the 1 SE confidence interval. 28
A.1 Parameters for the linear regression between $\log(\frac{CI_{95}}{MAD_{disp}})$ and log(N). 45
B.1 Mean of median centre flow line velocities and slope of lake-terminating and land-terminating glaciers in m/year for second half of the ablation zone. Uncertainty estimates represent the 1 SE confidence interval. . . 47

1 Introduction

The Himalayan mountains store vast amounts of snow and ice, ensuring a year-round supply of melt-water for downstream areas (Immerzeel et al., 2010; Viviroli et al., 2007). The Ganges and Brahmaputra rivers drain the majority of the Himalayas and more than half a billion people living along its tributaries, all relying in a varying degree on a stable water supply. A large decrease in runoff from these rivers will have major implications for downstream food security, in particularly in areas downstream of the Brahmaputra river (Immerzeel et al., 2010), with tens of millions of lives that will be threatened. Although for current projections drastic reduction in glacier area in the Himalayas over the 21th century are expected, large uncertainties in the pace of area loss exist (Lutz et al., 2013). Hence, large uncertainties in future melt water supply are evident, and an improved understanding of the evolution of Himalayan glaciers is urgently needed.

Himalayan glaciers have been retreating and loosing mass since the mid-19th century and rates of mass loss have been increasing over at least the last four decades (Bolch et al., 2012; Brun et al., 2017; Zhou et al., 2018; Maurer et al., 2019; King et al., 2019). Various studies report Himalayan averaged mas losses over glaciates areas of around 0.40 $\pm$0.10 m.w.e.a $^{-1}$ since the beginning of this century (King et al., 2019; Maurer et al., 2019), which roughly translates into a total mass loss of 7.5 Gt year^{-1}, or equivalently, about 3 million Olympic swimming pools, each year. However, within the Himalayan mountains, large intra-regional variability in glacier mass loss exists (Brun et al., 2017; Maurer et al., 2019; King et al., 2019). This indicates that there are factors capable of exacerbating -or slowing down- glacial mass losses that are at least partially decoupled from climate.

Considerable parts of the Himalayan glaciers, in particular below the snowline, are covered by a thick debris mantle. Debris has an important control on glacier ablation, and thus the glacier mass balance; A thin layer of debris accelerates melt as it has a lower albedo than debris-free ice, whereas a debris layer thicker than a few centimetres suppresses melt because its insulating properties start to dominate (Vincent et al., 2016; Evatt et al., 2015; Bisset et al., 2020). As a result, mass loss is often focused in the mid parts of the glacier ablation zones where debris cover is thin, causing localised surface lowering. This reduces the downglacier surface gradient, which in turn reduces driving stress and glacier velocity (Benn et al., 2012). As a consequence, the lower ablation zones of many glaciers are now stagnant (Quincey et al., 2009).

Despite the insulating properties of a thick debris layer, Kääb et al. (2012); Gardelle et al. (2013); King et al. (2019) and King et al. (2019) showed comparable thinning rates for debris-covered and clean-ice glaciers at similar altitudes, and in recent years it has been an ongoing debate to explain this 'debris cover anomaly' (Salerno et al., 2017; Brun et al., 2018). Several studies addressed this problem and suggested that supraglacial ponds and ice cliffs, which often form on low-gradient, stagnant parts of the ablation zone, considerably enhance glacier ablation and are responsible for the larger than expected elevation lowering (Immerzeel et al., 2014; Pellicciotti et al., 2015; Brun et al., 2016; Miles et al., 2016). On the other hand, Vincent et al. (2016) and Anderson and Anderson (2016) proposed that differences in emergence velocity between clean-ice and debris-covered glaciers might be responsible for the observed similar thinning rates. Unlike debris-covered glaciers, clean-ice glaciers often maintain an active flow far towards the terminus, showing a high emergence velocity (surface mass-balance rate minus emergence velocity) and could in such way sustain a contrasting mass balance under comparable tinning rates. However, debris-covered glacier fronts

have remained remarkable stable over the past decades (Bolch et al., 2008), which stands in stark contrast with clean-ice glaciers (Scherler et al., 2011b), and indicates that debris cover exerts a significant control on thinning rates for at least the area near the terminus. This is indirectly supported by the observed reduction in down-glacier surface gradient by King et al. (2018) in the mount Everest region.

Also the development of proglacial lakes are becoming an increasing topic of interest, as they are associated with enhanced glacier mass loss in the Himalayan region (King et al., 2018; Maurer et al., 2019; King et al., 2019). The number of proglacial lakes and supraglacial lakes in the Himalayan region has been rising and lakes have been growing in size (Zhang et al., 2015; Nie et al., 2017). This trend is likely to be ongoing in the near future, considering many glaciers preconditioned with areas of overdeepening (Linsbauer et al., 2016). Also, glaciers are often bounded by unstable ice-cored terminal moraines, with a large risk of a glacial lake outburst flood (GLOF) (Richardson and Reynolds, 2000; Rounce et al., 2015), which can have a devastating impact on downstream areas (Carrivick and Tweed, 2016).

The dynamics of glaciers that terminate into a body of water are widely studied in various settings in the arctic and alpine regions, and a great variety of shapes and behavior between water terminating glaciers is evident (Truffer and Motyka, 2016). Generally, glaciers terminating in fresh water exhibit frontal mass loss rates of a magnitude smaller than glaciers terminating in a comparable tidewater environment (Benn et al., 2007b). Nevertheless, ice mass loss rates in both settings have been shown to be elevated above land terminating glaciers at various places in the world (Truffer and Motyka, 2016; Willis et al., 2012; Tsutaki et al., 2016), and their flow characteristics have been found to be contrasting (Willis et al., 2012; Burgess et al., 2013). Therefore, a robust understanding of the dynamics of lake-terminating glaciers is crucial.

Most studies cover water-terminating glacier dynamics in the context of calving processes, as calving is often the dominant mechanism that removes large masses of ice at the water-glacier interface, accounting for a major contribution in the total water-terminating glacier mass balance. Ultimately, mass losses through calving (U_c), for now taken as the sum of mechanical mass losses and subaquaseous melt, depends on the velocity at the glacier terminus ($\overline{U}_T$) and the glacier length over time (dL/dt):

$$U_c = \overline{U}_T - \frac{dL}{dt} \tag{1}$$

Depending on the initial settings, a water body has yet to develop (alpine settings), or is already present (e.g. Marine outlet glaciers in Eastern Greenland, Antarctica, or large fresh water lake systems in Alaska and Patagonia). The dynamics of a glacier flowing into this water body can be kicked out of balance by either a further development of a proglacial lake or increased surface melt, and either of these processes eventually creates an increased buoyancy force, reducing the effective pressure at the glacier glacier-bed interface. If the dominant source of friction arrives from basal drag, as assumed in the first-order calving model from Benn et al. (2007b)(figure 1), a reduction in the effective pressure-dependent drag will result in an increased velocity at the glacier terminus, longitudinal stretching and consequently dynamic thinning. Dynamic thinning then reinforces the reduction of the effective pressure, resulting in a positive feedback on the glacier terminus velocity. Also, strain rates resulting from longitudal stretching results in the opening of transverse crevasses, making the ice more susceptible to calving. By this means positive feed-backs between thinning and longitudinal stretching can explain how thickness changes, flow acceleration, and calving retreat form a self-reinforcing cycle that can amplify glacier response to an initial

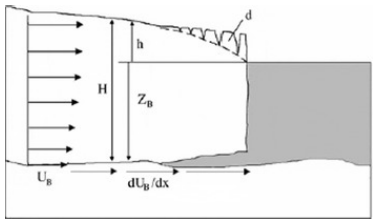

Figure 1: Schematic illustration of first-order calving in response to dynamic thinning. Surface crevasses propagate downward to some depth d in response to the velocity gradient $\partial U_B/\partial x$, which relate to the velocity at the surface. Terminus might be either floating or grounded (after Benn et al. (2007a)).

forcing (Vieli et al., 2001). Clearly, $\overline{U}_T$ and dL/dt are not independent variables, en therefore the dynamics of these glaciers can only be understood as an intricately coupled system (Benn et al., 2007b).

The above mentioned model shows some basic aspects that are able to explain how lake-terminating glaciers dynamically can diverge from a land-termination glacier onto an equal climatic forcing. However, it only partly can be applied to lake-terminating dynamics and neglects or highly oversimplifies some general aspects that are of major importance. For example, the model does not incorporate the resistance from lateral drag, which plays a significant role in the force balance of relatively narrow valley glaciers. Also, it neglects changes in the longitudinal stress gradient, which might exert a strong influence on glacier flow when glacier systems are undergoing rapid change (Benn et al., 2007b).

A factor that further complicates the dynamics and mass loss of lake-terminating glaciers is the presence of a thick layer of debris, of which plenty can found at the Himalayas (King et al., 2019). The low-gradient debris-covered part of many Himalayan glaciers acts as a sweet spot for proglacial lake development, which often result from a deepening and coalescence of supraglacial lakes (Quincey et al., 2007; Benn et al., 2012) and become bounded by an stagnant, ice-cored moraine dam. The combination of the morphology, insulating characteristics of debris and lake development may cause a responds onto climate forcing that is strongly non-linear (Benn et al., 2012), though only little is know how such a transition dynamically develops. Several studies observed calving (Kirkbride and Warren, 1999; Sakai et al., 2009; Watson et al., 2020) and the formation of transverse crevasses (Kirkbride and Warren, 1999; Sakai et al., 2009; Watson et al., 2020), indicating that also for debris-covered lake-terminating glaciers dynamic thinning has to be considered.

Regional observational evidence for contrasting behaviour between land-terminating and lake-terminating glaciers in the Himalayan mountains mainly arrives from remote sensed data through area reduction and glacier-wide geodetic mass balance (hereafter glacier mass balance) data. Enhanced glacier area reductions from lake-terminating glacier have been observed in the Sikkim Himalaya by Basnett et al. (2013), showing two times higher losses in glacier area than for glaciers without lakes, for both debris-covered and clean-ice glaciers. Contrasting area losses are also observed in the Everest region (King et al., 2017) and around the entire Himalaya arc, with lake-terminating glaciers showing increasing terminus retread rates over the last two decades (King et al., 2019).

Glacier mass balance data are calculated from the rate of elevation change. The first study quantifying the contrasting behaviour was restricted to the Everest region and showed 32% more negative mass balance for lake-terminating glaciers than land-terminating glaciers over the period 2000-2015 (King et al., 2017). More recently Maurer et al. (2019) presented a Himalaya-wide glacier mass balance dataset and showed 30% more negative glacier mass balance compared to the average over the period 2000-2016, which is in line with the 33% more negative than average Himalayan mass balance over 2000-2015 found by King et al. (2019). Over the same period a lake-terminating glacier mean mass balance was found that is 18% to 98% more negative than the Himalayan regional average (Brun et al., 2019), confirming that the contrasting behaviour is a regional wide phenomenon.

Regional indications for a contrasting dynamical behaviour, that is, difference in velocity regime, are very limited, predominantly indirect and mostly arrive from contrasting thinning rates at the glaciers front. King et al. (2019) observed that thinning rates are amplified at the lake-terminating termini, and attributes this to mechanical calving and subaqueous melt. Also this study speculates that the recent increase in thinning rates are related to an average increase in proglacial lake depth. Also Song et al. (2017) revealed substantial thinning trends at glacier lake termini over the period 2000-2014, though focusing his analysis on solely debris-covered, lake-terminating glaciers. A combined assessment on both elevation changes and velocity changes on nine land-terminating and nine lake-terminating, debris-covered glaciers in the central Himalayas showed for five out of nine lake-terminating glaciers substantial thinning, flow acceleration and increased longitudinal strain in their terminal zone (King et al., 2018). One recent study (Liu et al., 2020) examined in detail the interannual flow dynamics of the Longbasaba Glacier and observed a clear recent acceleration of the terminus since 2012, and hence showed clear evidence of dynamic thinning at this partly debris-covered glacier. However, a region wide analysis on contrasting dynamics between land-terminating and lake-terminating glaciers using surface velocity data is still lacking, and will contribute towards a better understanding of lake-glacier dynamics in the Himalayas.

Deriving glacier surface velocities from optical satellite imagery using image-matching methods is well established within glaciology. In its early days it involved manual identification of the same features in two images (Krimmel and Vaughn, 1987; Whillans and Bindschadler, 1988; Harrison et al., 1992), but became automated by the ongoing development of feature tracking techniques and was employed for the first time by Bindschadler and Scambos (1991) and used to derive glacier velocities of ice streams in Antarctica. In these early applications, a limitation common optical satellite imagery was that feature tracking required high-contrast surface features, such as highly crevassed areas, leading to patchy ice velocity retrievals. With the launch of Landsat-8 in 2013 many of these limitations where overcome, in particular due to its improved radiometric performance (12 bit compared to 8 bit), better geometric stability and higher acquisition rate. The launch of ESA's Sentinel-2 A/B satellites even further enhanced the monitoring of glaciers and land ice masses given the high temporal frequency of 5 days (compared to 16 days for Landsat-8). In addition, the higher spatial resolution of Sentinel-2 compared to Landsat-7/8 (10 m versus 15 m) is expected to capture more small glaciers, resulting in more detailed mapping of their surface speed.

The large amount of available remote sensing data has let to several larger-scale applications in the Himalayan region on glacier surface velocities. For example, Scherler et al. (2011b) produced centre flow line velocities for several parts of the Himalayan region by computing the mean of a stack of velocities obtained from feature-tracking

of 657 ASTER and SPOT images for the period of 2000–2008. Other studies used a complete archive of Landsat imagery to compute velocity fields for whole high mountain Asia (Dehecq et al., 2015, 2019a), resulting in the use of very large numbers of image pairs. Only few glacier surface velocity datasets that cover the entire Himalaya are openly available, with most notably the data provided by the NASA MEaSUREs ITS_LIVE project (Gardner et al., 2019) that produces yearly world-wide velocity mosaics from all available Landsat imagery from as early as 1985 untill present.

Studies on ice velocities that use sentinel-2 are largely limited to so-called 'showcase studies', focusing on the potential of the satellite for ice flow measurements (Kääb et al., 2016; Altena et al., 2019; Kääb et al., 2016). For example, Kääb et al. (2016) tested the potential of sentinel-2 imagery on multiple glacierized areas around the world and reported that ice velocities can be measured with accuracies down to 1-2m for repeat-orbit, stating its potential as 'impressive'. To our knowledge, only one study so far used sentinel-2 imagery on high mountain Asia, examining a glacier surge on the Shispare Glacier at the Karakoram (Bhambri et al., 2020). Also, the only region wide study using sentinel-2 imagery stems from the Copernicus Glacier Service and calculated 2018 glacier ice velocities for the whole mainland of Norway (Nagy and Andreassen, 2019). Despite its clear potential a regional wide velocity dataset for the Himalayan region based on Sentinel-2 imagery hasn't been deployed until this day, and could be highly valuable for several applications, such as investigating contrasting dynamics between lake-terminating and land-terminating glaciers.

2 Objectives

The main objective of this study is to examine the influence of proglacial lakes on Himalayan glacier dynamics, in order to improve the current understanding of the large subregional heterogeneity of glacier behaviour. In more detail, we seek to attribute lake-driven changes in the velocity field to dynamic thinning and investigate the role that debris cover on glacier-lake dynamics plays. For this we employ the Sentinel-2 satellite to derive a large-scale contemporary Himalayan glacier velocity dataset at an improved resolution compared to existing studies so far. We compare the velocity dataset against surface elevation change data from King et al. (2019), together with other basic glacier features, to discuss the role of proglacial lakes and debris cover on glacier dynamics and their potential to accelerate current and future mass losses.

3 Study Area

Our study area covers five different subregions within the Central and Eastern (CE) Himalaya (fig. 2). Glaciers in the CE Himalaya cover an area of ∼13,900 km^2, wich is about 60% of the glacierized area at the total Himalayan arc (Bolch et al., 2012). The Himalaya are located around the southern rim of the Tibetan Plateau (TP), and the CE Himalaya are the source of two major trans-boundary rivers, namely the Ganges and the Brahmaputra. The CE Himalaya receive more than 80% of its precipitation during the the Indian summer monsoon, stretching from from May to October (Bookhagen and Burbank, 2010), and consequently all glaciers are of 'summer accumulation type' (Ageta and Higuchi, 1984). Also, the extreme Himalayan topography exerts a strong influence on north-south contrasting precipitation patterns by forming an orographic barrier and depleting the monsoonal air of the bulk of the moist a the southern windward slopes, resulting in relatively dry slopes down the TP.

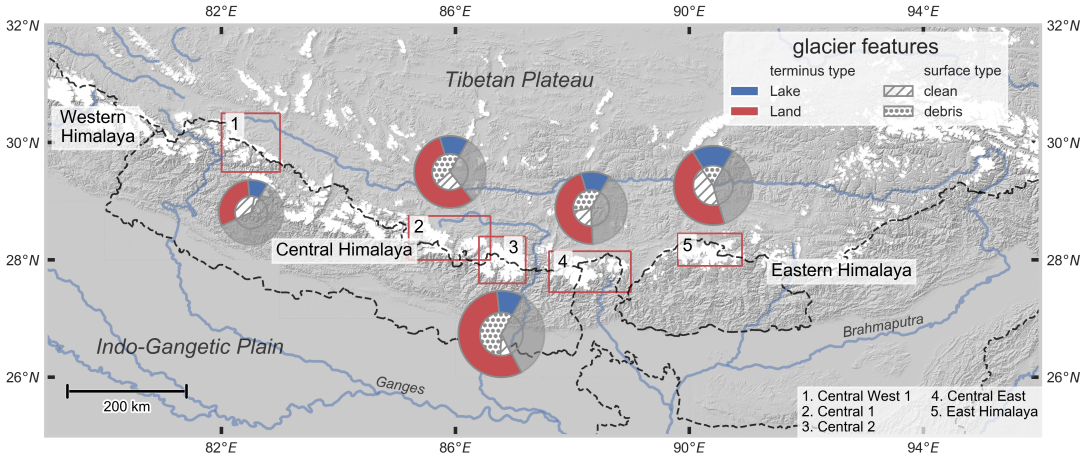

Figure 2: Map showing the regional subdivisions (red rectangles) and the associated glacier characteristics (pie charts), including terminus type and surface cover as a fraction of the total sub-regional glaciated area. The size of the pie charts correspond to total size of the sub-regional glaciated area, with largest areal ice cover found in Central West 2 (1404 km^2) and smallest in Central West 1 (920 km^2). Transparent fractions of the pie charts represent the area that is not covered in in study. Transboundary rivers are indicated by blue lines, whereas glacier areas are colored white. Country boundaries are tentative and for orientation only. This figure was generated using Matplotlib, vers. 3.1.2, together with Python, vers. 3.7.

Related to this is a stark contrast in north-south relief is the distribution of clean-ice and debris-covered glaciers (Scherler et al., 2011a). Glaciers in low-relief areas sloping northwards facing the TP generally show little or no debris cover and have extensive accumulation areas. In contrast, glaciers surrounded by much steeper topographies receive a large proportion of their accumulation by snow avalanching from steep hillslopes. Steep hillslopes supply large fluxes of rocky material to the glacier

Table 1: Regional distribution of lakes-terminating glaciers and debris-covered glaciers. The numbers without units represent the number of glaciers withing a specific glacier category, with the percentages showing the relative fraction of surface area the subselection occupies within the subregion. The area column shows the area that glaciers of our selection occupy in each subregion, and the coverage being the percentage of the total glacier areal occupation of our glacier selection. The coverage over the whole region (41%) is relatively low since it also incorporates all CE Himalayan glaciers outside our subregions.

	Terminus Type		**Surface Cover**			
	Number, (% Area)					
Subregion	Lake	Land	Debris	Clean	Area	Coverage
Central West 1	6 (24%)	33 (76%)	7 (12%)	32 (88%)	920 km^2	40%
Central 1	16 (18%)	53 (82%)	36 (66%)	33 (34%)	1098 km^2	69%
Central 2	10 (15%)	57 (85%)	44 (87%)	23 (13%)	1404 km^2	66%
Central East	17 (21%)	57 (79%)	34 (62%)	40 (38%)	1130 km^2	59%
East Himalaya	20 (27%)	49 (73%)	19 (29%)	50 (71%)	1238 km^2	63%
All	70 (21%)	249 (79%)	139 (57%)	178 (43%)	5781 km^2	41%

and as a result glaciers in such settings often have an extensive debris cover, which can range from a few centimeters to several meters (Gardelle et al., 2011; Scherler et al., 2011a).

In this study we only focus on glaciers with a area larger than 3km^2, which is done for several reasons. Firstly, small glaciers are often clean, located at a high elevations, do typically not host a proglacial lake and thus fall out our field of interest. Secondly, small glaciers often show only very low surface velocities, and if they do, contain high amounts of shear, which cannot be captured by the limited resolution of available optical satellite imagery. Note that in general glacier volume scales exponentially with glacier surface area, which increases the representativeness of our study onto potientiall ice volume losses.

In order to study glacier-lake dynamics, we select five subregions within the CE Himalayas with high density number of proglacial lakes, following the lake inventory of Zhang et al. (2015), and for the regional subdivisions and naming convention we follow the study of King et al. (2019) (table 1, fig. 2). We classify glaciers as lake-terminating when the glacier is in direct contact with the water front, and base our classification on the glacial lake inventory of Zhang et al. (2015); Wangchuck and Bolch (2020, in press) and manual optical based classification using multiple sources of satellite imagery. We do not classify glaciers that host supraglacial lakes as lake-terminating as we cannot be certain of the depth of these lakes and whether they are directly influencing glacier behaviour. Also the classification of debris cover is binary (debris-covered or clean-ice) and for this we follow the criteria defined by King et al. (2019) and Brun et al. (2019), classifying glaciers as debris-covered where more than 19% of their area was mantled by debris.

The smallest subregion, Central West One, is located in northwest Nepal bordering China, and has a relatively low glaciated area coverage (40%) resulting from the relatively high amount of small glaciers in the area. Most of the glaciers in the dataset are clean, flow north onto the TP, and a small proportion of the glaciers (6 out of 39)

terminate into a lake, but take up a relatively large proportion of the covered glaciated surface area (25%). Subregion Central 1 includes the mountain massifs located around the Poiqu river basin, bordering Nepal and China. A large proportion of the glacier population have ablation zones with an extensive debris cover, and the majority of clean-ice glaciers flow onto the Tibetan plateau, with a large fraction terminating into lakes. Central 2 covers the largest glacierized area (1404 km^2) and includes the Mt. Everest, bordering again Nepal and China. Most glaciers are debris covered (44 out of 67) and take up a disproportionately large part of the covered surface area (85%). Also most lake-terminating glaciers are covered by a layer of debris. Subregion Central East is located in the Sikkim region, bordering Nepal, China and India, and shows a great variety of clean-ice, debris-covered, lake-terminating and land-terminating glaciers. At last, East Nepal covers most of glaciated area in Bhutan, including some significant ice fields. Here, generally large clean glaciers flow north onto the TP of which many are lake-terminating, but also several debris-covered lake-terminating glaciers can be found in the mountain range interior. In total, our glacier dataset covers 41% of the total glaciated area in the CE Himalayas.

4 Methodology

In this chapter we will start with a description of the processing strategy towards the glacier surface velocity field (Section 4.1), which involves a overview of the relevant Sentinel-2 image specifications (Section 4.1.1), image pair selection process (Section 4.1.2), preprocessing the satellite images (Section 4.1.3), description of the image-matching (Section 4.1.4) and finally a presentation of the postprocessing workflow (Section 4.1.5). Next, we will describe our strategy to asses the precision and uncertainty of the surface velocity flow field in Section 4.2. In Section 4.3 we will introduce other datasets used in our analysis, namely the glacier surface elevation change (after King et al. (2019)) and estimations of the equilibrium-line altitude (ELA). Finally, we present a strategy to analyse centreline data (Section 4.4), to calculate the glacier surface slope (Section 4.5) and to asses the uncertainty of regional mean velocity quantities (Section 4.6).

4.1 Surface Velocity

4.1.1 Sentinel-2 Specifications

The European Copernicus Sentinel-2 satellite series consist of two satellites; Sentinel-2a, launched in June 2015 and Sentinel-2b, launched in March 2017. Both Sentinel-2 satellites carry the Multispectral Instrument with an 290km swath width and 13 spectral bands spanning from the visible and the near infrared to the short wave infrared (Drusch et al., 2012). The highest spatial resolution bands are at 10m; three in the visible and one in the near-infrared (VNIR) spectrum. The two satellites are placed in the same sun-synchronous orbit and have a combined revisit time of 5 days but obtain a higher effective revisit time at mid latitudes due to overlapping swaths.

The raw granules of 25km cross-track and 23km along-track from the individual pushbroom modules are mosaicked and ortho-rectified using PlanetDEM 90 which is a multi-source elevation product processed from SRTM data version 4.1. These orthorectified products (Level-1C) are then clipped to 100km by 100km tiles in UTM/WGS84 projection and freely available at https://earthexplorer.usgs.gov/. In this study we use the 10m VNIR band (band 8) as fresh snow, clean ice and old firn show a wide contrast in their spectral properties at this wavelength and proved to work generally well for feature tracking on a variety of glacier surfaces (Kääb et al., 2016).

Throughout most of its mission, the multi-temporal co-registration accuracies of Sentinel-2 products from the same orbit stayed below 12m ($CI_{95.5}$), which is monthly reported by the European Space Agency (ESA). When co-registering two Level-1C images from the same relative orbit (repeat-orbit), DEM effects will be present but have the same pattern in both data sets (because they have a similar off-nadir cross-track look angle) so that they can easily partly be eliminated by calculating the average offset field obtained from correlating the two images. Products acquired from neighbouring overlapping swaths translate into additional offsets of up to 5.9m (Kääb et al., 2016), and will therefore be omitted in this study.

4.1.2 Image Pair Selection

We aim for a velocity field that is spatially complete, with different types of glacier surfaces (i.e. fresh snow, debris) being well represented. Selecting only one image pair will likely result in many outliers and gaps in the velocity field due to shadows, residues of clouds, low visual contrast or sensor saturation. Particularly obtaining

Table 2: An overview off all the November Sentinel-2 number of images, image pairs and effective date between 2016-2019 for every image tile used in this study.

Satellite Tile	**N. of Images**	**N. of Pairs**	**Effective Date**
T44RPU	15	46	16-10-2018
T44RPT	16	58	28-10-2018
T45RTN	14	39	07-07-2018
T45RTM	13	34	25-05-2018
T45RUM	12	26	08-07-2018
T45RVM	19	76	20-09-2018
T45RVL	12	29	31-05-2018
T45RWL	11	25	01-07-2018
T45RXL	11	22	23-09-2018
T45RYM	13	34	09-10-2018
T46RBS	13	38	09-12-2018
total	149	427	24-08-2018

a complete surface velocity field on glacier areas with low visual contrast can be a challenge, especially because this is a common feature at fresh snow surfaces above the snowline (Heid and Kääb, 2012). Selecting several pairs of the same tile should partly bypass these problems, as they might be complementary, allowing a more spatially complete estimate of the velocity field. The final velocity field is then an average of all the valid velocity estimates, a strategy explored by several studies (i.e. Willis et al., 2012; Scherler et al., 2011a; Dehecq et al., 2015). Also, thanks to the Central Limit Theorem, multiple velocity estimates gives us an opportunity reduce the uncertainty in the velocity field (Section 4.2).

We select pairs separated by one year to produce an annual velocity field. We solely take this one-year interval, and not, for example, a sum of half year intervals, because similar seasons often result in similar surface conditions which improves the image matching algorithm between image pairs. Also, the presence of the Indian summer monsoon largely restricts us to a small time window of low cloud cover. Lastly, generally low snowline during winter months, covering vast areas by fresh snow, further restricts a suitable time window for image matching, and we subsequently only select images for the month November.

After the launch of Sentinel-2a in June 2015 Level-1C images were not directly available as the satellite was still in his 'ramp-up' phase, resulting in a very incomplete satellite archive. This leaves us with a maximum of 3 satellite images for November 2016, and 6 for the consecutive years 2017-2019 after the launch of Sentinel-2b. We obtain an annual velocity field of year T by selecting all pairs of the form (T 1; T) and (T; T + 1), and thus each image is paired with up to 12 other images. However, this maximum is often not reached, as we remove images with high cloud cover over glaciated areas manually from our satellite archive. In total this results in a dataset of 149 images and 427 image-pairs with a effective date at 24-08-2018 (table 2). Note that due to the lower repeat cycle in 2016, this date is centered towards the end of the November 2016 - November 2019 interval.

4.1.3 Preprocessing

Stumpf et al. (2018) presented a processing workflow that significantly reduces the coregistration error down to below 3m, and intuitively a reduction of this error at this processing phase seems wishful. However, to reduce computational costs we choose to eliminate this error not at this stage but after the postprocessing phase. Note that this only tackles systematic offset between the image pairs and not the offset between pushbroom modules, but this is expected to be about an order of magnitude smaller (Kääb et al., 2016). In order to significantly reduce the computational costs, a mask is applied over all the non-glaciated areas and glaciers with an area below 3km^2. For this mask we use the glacier outline database from The Randolph Glacier Inventory (RGI 6.0) (The RGI Consortium, 2017). Next to this mask, we select in every tile an area off-glacier off about 300km^2, where the displacement is expected to be zero, as firstly, we will use it to assess the precision and uncertainty of the feature tracking algorithm and secondly, to reduce the co-registration error (Section 4.2).

Heid and Kääb (2012) evaluated several feature tracking methods and showed that a method called 'orientation correlation' performed best under most circumstances. This method, developed by Fitch et al. (2002), creates two orientation images, f_0 and g_0, from image pair $f(t)$ and $g(t+1)$ by:

$$f_0(x,y) = sgn\left(\frac{\partial f(x,y)}{\partial x} + i\frac{\partial f(x,y)}{\partial x}\right) \tag{2}$$

and

$$g_0(x,y) = sgn\left(\frac{\partial g(x,y)}{\partial x} + i\frac{\partial g(x,y)}{\partial x}\right) \tag{3}$$

where

$$sgn(x) = \begin{cases} 0 & if \quad |x| = 0 \\ \frac{x}{|x|} & otherwise \end{cases} \tag{4}$$

Each pixel in a orientation image is a complex number. Each complex number represents the orientation of intensity gradient at that pixel. The magnitude of a pixel is either one or, in the case of a uniform region of the image with no gradient, zero. Since correlation is used for matching, a 0 + 0i pixel will have no effect. This is a desirable property, as uniform area of an image provides no information for a match, making the method invariant to illumination change.

4.1.4 Image matching

From the two orientation images $f_0(x,y)$ at time t and $g_0(x,y)$ at $t+1$ a search chip $f_c(i,j)$ and a reference chip $g_c(i,j)$ centered around the same location (x,y) are extracted. The search and reference chip are matched using correlation. Correlation is computed in the frequency domain with Fast Fourier Transforms (FFTs), according to the convolution theorem (McClellan et al., 1999). Given $F_C(k,l)$, the FFT of $f_c(i,j)$, $G_C(k,l)$, the FFT of $g_c(i,j)$, and IFFT() the Inverse Fast Fourier Transform function, the orientation correlation $CC(i,j)$ matching surface is:

$$CC(i,j) = \Re\Big\{IFFT\big(F_C(k,l)G_C(k,l)\big)\Big\} \tag{5}$$

The registration of $f_c(i,j)$ and $g_c(i,j)$ is measured from the position of the maximum in $CC(i,j)$. Concretely, we match the orientation of the intensity gradient that is contained in the phase of the orientation image. After this initial estimate we then refine the maximum estimation by upsampling the product $F_C(k,l)G_C(k,l)$ only in a small neighbourhood of the initial maximum (Guizar-Sicairos et al., 2008). Note that the resolution of the algorithm depends on the size of the reference chip g_c. Also, because of the cyclic nature of the FFT, shifts greater than half the image size have four possible interpretations of the maximum and therefore such matches should therefore be avoided. Consequently the maximum search area is equivalent to half the search chip size f_c. Also note that the algorithm assumes that f_c and g_c are the same size. This problem can easily be circumvented by zero padding the smaller size chip g_c to the size of the larger chip f_c prior to taking the forward FFTs. This matching process is repeated over all the glaciated areas with steps equalling half of the search chip size, for all image pairs. This leaves us with n-pairs of velocity data matrices (x- and y-displacement) with a resolution of $0.5 \times width_{g_c}$ for each given satellite scene.

Several important parameters are summarized in table 3, of which a few have to be addressed in more detail. The choice of the reference chipsize is the most important one since it must be large enough to avoid correlating only noise but small enough to resolve shear at the glacier surface. For this we lean on available literature and, use a 16 by 16 pixel chip (Dehecq et al., 2015; Gardner et al., 2019), which results in a matching window of 160m by 160m. The search limit must be chosen in such way that largely all velocity displacements in the region are captured, but should be kept small enough the avoid needless computational costs, hence we set our search limit to 230m.

4.1.5 Postprocessing

The velocity fields contain match blunders that need to be removed. Here we largely adopt a strategy proposed by Gardner et al. (2020). We use a disparity filter that is composed out of two components. First, a the filter checks for the 'uniqueness' for each component velocity by comparing each element with there surrounding neighbours that are co-located in a 5 by 5 kernel. If less than 9 of the 25 co-located are similar withing a 25% range of the search limit of the algoritm, the velocity component is considered to be too unique and is thrown out. The advantage of this filter is that it allows a velocity distribution that is bimodal, something which in not uncommon at glaciated areas where shear is very high. Secondly, a velocity component is also considered to be a blunder when it deviates more than three times the interquartile range from the median of all co-located pixels. This disparity filter is then repeated two times over the same area to make sure that all outliers are removed in areas that are blunder-abundant. Where possible, missing values are interpolated using the local median of a 3 by 3 kernel. Lastly, the whole algorythm is repeated from section 4.1.4 with a doubled chip size to fill the area with velocity estimates where the original chipsize failed.

For each 100 by 100 km tile we selected a large stable area for which we now can calculate the median offset in x- and y-direction. As we know that the average displacement field should be virtually zero, we expect any offset to be related to the coregistration error. Therefore, to reduce the noise in the velocity data, we subtract this median offset from the whole (glaciated and stable) x- and y-displacement field. The 2017-2019 final x- and y-displacement field is then created by taking the median of all the image pairs for both velocity components.

Table 3: Parameters used for image matching and postprocessing. Image matching parameters are given in Sentinel-2 pixel resolution units (10m), whereas postprocessing parameters are given in velocity pixelsize units (80m). *Unitless parameters, see Section 4.1.5 for context.

Image Matching Parameters	**size (image pixels)**	**size (m)**
Search Chipsize	16×16	160×160
Reference Chipsize	46×46	460×460
Search Limit	23	230
Iteration Step	8	80
Subpixel Resolution	1/16	0.625
Velocity Pixelsize	8	80
Postprocessing Parameters	**size (velocity pixels)**	**size (m)**
Filterkernel	5×5	400×400
Uniqueness Threshold	$1/4 \times 23$ *	
Uniqueness Limit	8 *	
MAD Threshold	4 *	
Interpolationkernel	3×3	240×240

4.2 Assessing the Precision and Uncertainty of the Velocity Field

4.2.1 Precision: Median Absolute Deviation (MAD)

The x- and y-displacement fields have likely a long-tail distribution through the contamination of residing outliers (Burgess et al., 2013). The usage of the standard deviation and mean relies too heavily on a normal distribution, and a robust alternative estimator is required. Therefore we use the median and median absolute deviation (MAD) as most important statistical indices (Dehecq et al., 2015), with the MAD at stable areas defined as follows:

$$MAD_{off} = 1.483 \times med_{(i,j)\in\omega_{off}}(\{|V(i,j) - \overline{V}_{off}|\}) \tag{6}$$

where

$$\overline{V}_{off} = med_{(i,j)\in\omega_{off}}(\{V\}) \tag{7}$$

and where ω_{off} is the ensemble of points at the stable area selection of each displacement tile. The scale factor 1.483 is used in order to use the MAD as a consistent estimator for the standard deviation, and assumes that the true distribution (distribution without outliers) is close to normal (Leys et al., 2013). As we noted in previous section, we expect $\overline{V}_{off}$ to be zero, hence we use this average offset as an estimator for the coregistration error. We estimate the dispersion, which is the MAD at each velocity location, by:

$$MAD_{disp}(i,j) = 1.483 \times_{t\in T} \{|V(i,j,t) - \overline{V}(i,j)|\} \tag{8}$$

where

$$\overline{V}(i,j) =_{t \in T} \{V(t)\} \tag{9}$$

and where T is the set of N velocity estimates at pixel (i,j) and depends on the number of image pairs and successful displacement retrievals. This is indicative of the variability between the different velocity estimates.

4.2.2 Uncertainty: 95% Confidence Interval (CI_{95})

Uncertainties of the final median velocity field are dominated by the precision of the feature-tracking algorithm, the coregistration error, the temporal variability of glacier flow and the number of velocity estimates. For a normal distributed population, the sample median converges to a normal distribution for an increasing number of velocity estimates (Chu and Hotelling, 1955). We previously dismissed the hypothesis of a normal distribution, but since the different estimations are independent and symmetrically distributed, we expect the 95% confidence interval of each median velocity component to follow a similar law (Dehecq et al., 2015):

$$CI_{95} = \kappa \frac{MAD_{disp}}{N^{\alpha}} \tag{10}$$

where MAD_{disp} is the dispersion at each velocity location of the N number of estimates and CI_{95} is the 95% confidence interval. Parameters κ and α determine the width and the thickness of the tail of the distribution and have yet to be determined. Eq. 10 leaves us with three unknowns, but can be solved at stable areas where CI_{95} can be determined as an function of MAD_{disp} and N, using the following logarithmic relation:

$$log(\frac{CI_{95}}{MAD_{disp}}) = log(\kappa) + \alpha log(N) \tag{11}$$

With this regression parameters κ and α can be calculated for each tile location with its corresponding stable area, employing this study with an uncertainty estimation for areas with actively flowing ice.

4.3 Surface Elevation Change and Estimation of ELA

We examine ice thinning rates using the surface elevation change (dh/dt) dataset from King et al. (2019), providing a continuous coverage of our study area at a 30m resolution. The dh/dt field is a mean estimate using 499 of the DEMs generated from WorldView and Geoeye optical stereo pairs spanning the period 2012-2016 and with an effective date around mid-2015.

In this study we focus our analysis on the ablation zone of glaciers, as we assume that glacier-lake dynamics are confined to the lower glacier reaches. For this we need an estimation of the equilibrium-line altitude (ELA), for which we follow the best available approach of Braithwaite and Raper (2009) in using the median altitude of each glacier. The median altitude, separating the lower and upper 50th percentile in surface area, and are made available by the RGI 6.0 (The RGI Consortium, 2017). The approach is well suited for glaciers that are in mass balance (Braithwaite and Raper, 2009), an assumption we clearly cannot make given the overall negative mass balance of Himalayan glaciers, leading to an underestimation of the ELA. Also, the RGI outlines do often not include entire accumulation zones that positively contribute to the mass balance by avalanching, resulting in an overestimation of the ELA (Benn

and Lehmkuhl, 2000). Consequently, debris covered glaciers are most susceptible for ELA inaccuracies.

4.4 Glacier Centre Flow Line Analysis

We analyse the velocity, dh/dt and slope (Section 4.5) along the main glacier centre flow line, an approach adopted by many previous studies (e.g. Scherler et al., 2011b; Nagler et al., 2015; Liu et al., 2020). Glacier centre flow lines are produced with the Open Global Glacier Model (OGGM) (Maussion et al., 2019) using a slightly adapted algorithm from Kienholz et al. (2014), glacier outlines from RGI 6.0 and the SRTM DEM. All centre flow lines are manually adapted using 2019 Sentinel-2 satellite data and velocity data from this study to ensure that the lines end at the 2019 terminus position and that they follow the main flow tributary.

To extract centre flow line velocity data we conduct a nearest neighbour sampling every 80 meters, and average the velocity estimate $u(i,j)$ by using the following 3 by 3 (240m by 240m) Gaussian window:

$$u_c = \sum_{j,i=-1}^{1} \frac{u_{i,j}}{(CI_{95_{i,j}})^2} e^{-\frac{1}{2}\frac{i^2+j^2}{\sigma^2}} \tag{12}$$

where $\frac{1}{(CI_{95})^2}$ is the weighting factor and σ=0.7, which is the standard deviation of the Gaussian window. Similarly follows the propagation of the uncertainty:

$$CI_{95,c} = \sum_{j,i=-1}^{1} \frac{1}{(CI_{95_{i,j}})^2} e^{-\frac{1}{2}\frac{i^2+j^2}{\sigma^2}}. \tag{13}$$

This approach increases the overall confidence of our median velocity estimates. Also, the Gaussian window prevents pixels further away from the centre flow line to have a high impact on the averaged data, which otherwise may have resulting in an underestimation of the velocity values.

Then, to compare the velocity profiles for multiple glaciers at the ablation zone, we select all velocity data starting at the ELA and upsample all glaciers with a ablation length below 4000m and downsample the rest. We take 4000m as the most representative length since the results will show that this approaches the overall median length of the ablation zone for the whole glacier population. The same approach is applied on the dh/dt dataset, which the only difference being that values are not weighted by the uncertainty.

4.5 Glacier Surface Slope

To calculate the slope of the ablation zone we use the Advanced Land Observing Satellite (ALOS) World 3D DEM (Tadono et al., 2014), which is available at a 30m resolution and spans the period 2006-2011. We calculate the slope (in degrees) of the glacier ablation zone by:

$$S_{abl} = tan^{-1}\big(mean_{x\in\omega_{abl}}(s_c(x))\big) \tag{14}$$

where ω_{abl} is the ensemble of slopes s_c(m/m) along the glacier centre flow line, which is calculated as follows:

$$s_c(x) = \left(\frac{z_c(x+dx) - z_c(x-dx)}{2dx}\right) \tag{15}$$

where z_c is the elevation at point x along the glacier centre flow line. Elevation points are extracted at the glacier centre flow line in a similar fashion to dh/dt (section 4.4). In this study we will only examine the slope for the whole or half the ablation zone, because slope calculations at small scales tend to become noisy (King et al., 2018).

4.6 Glacier Group Uncertainty

The glacier group uncertainty depends on the uncertainty of the individual glacier velocity points ($\mathrm{CI}_{95,c}$), the spread between the velocity points u_c among the sample group and the number of velocity points (N_u). We estimate this uncertainty by applying a Monte Carlo simulation by drawing 200 times a random sample from the uncertainty distribution of each individual velocity point u_c in the region of interest. Then for each sample round, following the bootstrap method, we draw N_u times a sample with replacement to calculate the median, and repeat this 500 times. This leaves us with 10^5 estimates of the median from which we determine the one standard error (SE) interval and we will use this as primary estimator of our regional mean velocity uncertainty.

5 Results

Fig. 3 gives an impression of the total 2017-2019 velocity field. We will start this chapter by assesssing the algorithm performance and uncertainty of this velocity field (Section 5.1), followed by a comparison of the velocity field with other regional studies 5.2. Then, we move to an analysis of the centre flow line velocities, first with an examination of the terminus type variability in velocity (Section 5.3), followed by an analysis of the role of debris cover on glacier-lake dynamics (Section 5.4-5.5).

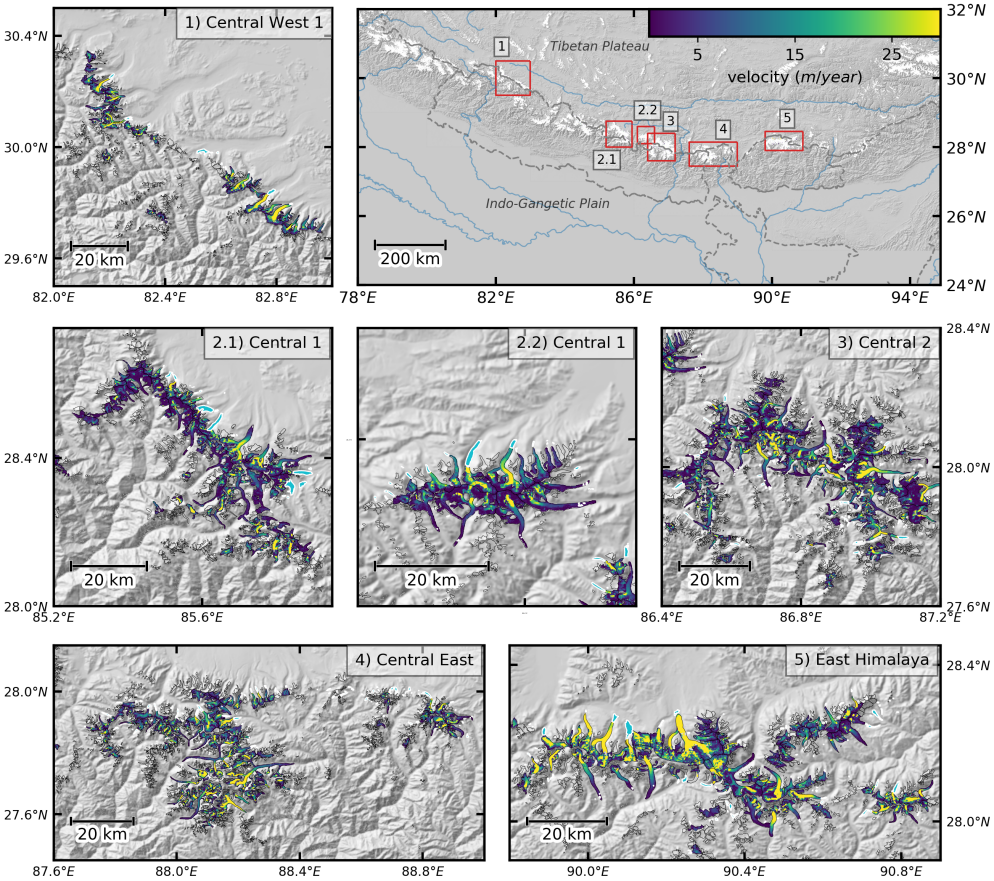

Figure 3: Regional 2007-2019 velocity fields across the Himalaya, with an illustrative distribution of water bodies (blue polygons, after Wangchuck and Bolch (2020)). Subregion Central 1 is for aesthetic reasons separated into two figures. Country boundaries are tentative and for orientation only. This figure was generated using Matplotlib, vers. 3.1.2, together with Python, vers. 3.7.

5.1 Algorithm Performance and Velocity Uncertainty

We find the absolute offset error of the median in the stable areas, $\overline{V}_{off}$ (eq. 7), to be below 14.04m (CI_{95})(fig. A.2) and this roughly agrees with the coregistration error reported in the monthly Sentinel-2 L1C Data Quality Report (Clerc, 2020). Remarkably, for the majority of image pairs the resultant MAD_{off} equals 0.93m/year for both the x and y velocity components, which is exactly $1.483 \times 0.625m$ (eq. 6). This implies that 50% of all the velocity estimates fall within the boundary of the subpixel resolution (0.625m) (fig. 4) and consequently to a large extent limits the overall very high algorithm performance at stable areas. We foresee that this limit will not cause resolution issues on glacier areas because firstly, a merge of multiple image pairs can yield certainty to a higher resolution than 0.625m, secondly, we are not focused on detailed velocities in the order of 1m and thirdly, other higher-order errors will likely dominate (Kääb et al., 2016). Note that our stable areas stretch 30 to 50 km (varying per tile location) in its longitudinal dimension and cover at most three individual pushbroom modules, and possible this study failed to capture errors between pushbroom modules, which are typically about 1 to 2m (Kääb et al., 2016). Also note the very small proportion of interpolated values centered around the zero median (fig. 4).

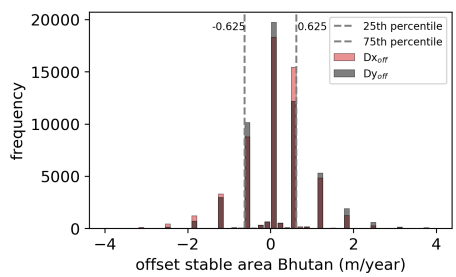

Figure 4: Spatial Median Absolute Deviation for both velocity components at a stable area (MAD_{off}) for a single image pair at East Himalaya. The 0.625m periodic distribution results from choices on the subpixel resolution. The vertical dashed lines define the interquartile range. Note that the velocity components largely overlap. For the location of the stable area see fig. A.1

For the glacier areas, the coregistration error enabled us to reduce MAD_{disp} by 56%, resulting in a MAD_{disp} distribution with a median at 4.15 m/year (fig. 5a). The distribution is heavy-tailed, with largest uncertainties found at accumulation zones where the algorithm was unable to remove all mismatches (fig. A.3). Another large source of uncertainty is the interannual variability in glacier flow, resulting in high dispersion in areas with an overall high flow velocity.

The parameters resulting from the regression between $log(CI_{95}/MAD_{disp})$ and $log(N)$ (table A.1) allows us to compute the 95% confidence interval (CI_{95}) as a function of MAD_{disp} and number of valid estimates N. This results in a distribution with an overall the shape that is very similar to the distribution of MAD_{off} (fig. 5b), but is now weighted against N, which is particularly low in accumulation areas where saturation issues occur. The CI_{95} distribution is slightly less heavy-tailed than MAD_{disp}, with a median uncertainty just below 3m.

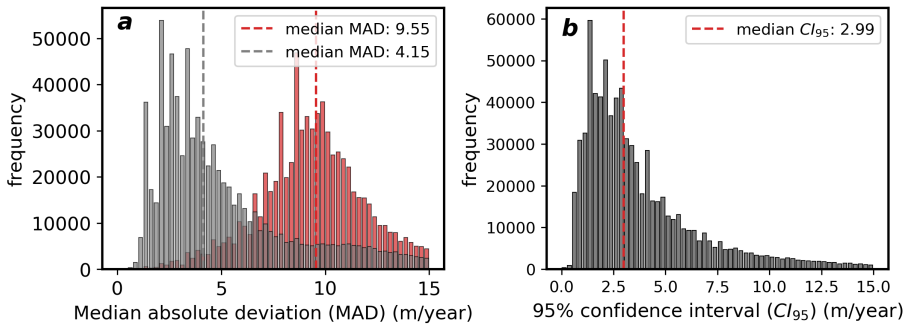

Figure 5: Dispersion (MAD_{disp}) (a) and 95% confidence interval (CI_{95}) (b) at glacier areas. (a) The red distribution represents the MAD_{disp} before subtracting $\overline{V}_{off}$ from each image pair, which realized a 56% reduction of the median dispersion, resulting in the grey dispersion distribution. (b) CI_{95} resulting from the estimated distribution of median displacement vector as a function of the number is velocity estimates and MAD_{disp} (eq. 11).

When evaluating the CI_{95} along the centre flow lines, a consistent trend is shown (fig. 6). The uncertainty decreases from the ELA moving further in to the ablation zone through the enhanced pixel contrast. Close to the terminus however, the uncertainty slightly shoots up due to relatively large interannual changes in surface properties, resulting in reduced algorithm performances. Interestingly, lake-terminating glaciers have consistently higher uncertainty along the ablation zone, which likely results from the large velocity differences between lake-terminating and land-terminating glaciers (Section 5.3). In the following sections we consider velocity estimates with a CI_{95} larger than 5 m/year as too uncertainty, and these estimates will be left out in further analysis.

5.2 Comparison with Previous Studies

The lack of ground-truth velocity measurements hinders simple evaluation of remotely sensed measurements in most cases (Scherler et al., 2008). Yet, in order to assess the quality of the measurement we found two region wide velocity datasets, both processed with predominantly optical Landsat-8 imagery. Dehecq et al. (2019b) produced a composite glacier surface velocity for the Pamir-Karakoram-Himalaya for the years 2013-2015. Velocity fields are available at 120m resolution and produced using a 240m reference window (Dehecq et al., 2015). Another region wide dataset is generated using auto-RIFT (Gardner et al., 2020) and provided by the NASA MEaSUREs ITS_LIVE project (Gardner et al., 2019). This velocity field spans from 1985 to 2020 with and effective date varying around spring 2018, is available a 120m resolution and again is computed using a 240m reference window.

Fig. 7 shows the comparison of the region wide median centre flow line velocity between our dataset and the two aforementioned datasets. All the velocity fields are analyzed following the exact same method as described in section 4.4. Remarkably larges differences in median velocity between the three studies exist, with maxima ranging from just above 5 m/year (Gardner et al., 2019) to well above 13 m/year in

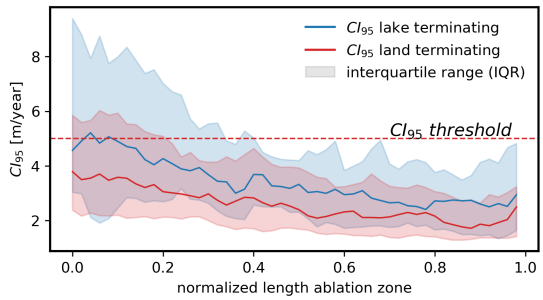

Figure 6: Median CI_{95} (m/year) for lake-terminating glaciers (blue) and land-terminating glaciers (red) along the normalized glacier centre flow line at the ablation zone, with the terminus positioned at the right end of the figure. The spread among the glacier population is represented by the interquartile range (IQR). The numbers shown at the legend indicate the population size. All centre flow line velocities with CI_{95} >5m/year are eliminated.

our study. Studies do agree reasonably well close to the terminus (within 0.5m/year range) where median velocities are expected to be close to stagnant, which indicates that differences between flow fields are proportional to the magnitude of the regional median centre line velocity. We propose two possible explanations for this discrepancy. Firstly, Dehecq et al. (2019a) observed over this current century a slowdown for all our subregions, ranging from $-14.5 \pm 1.3\% to - 21.0 \pm 2.3\%$ per decade and relates this to climate induced changes in slope and ice thickness, which could partly explain the differences in velocity between Dehecq et al. (2019b) and Gardner et al. (2019). Secondly, glaciers in the Himalaya can be down to 400m in width and consequently the lateral stress induced transverse velocity gradient can be substantial. A reference window size g_c of 240m might result in an underestimation of the centre flow line velocity as it is simply unable to resolve this velocity gradient. We therefore argue that the higher velocities in our study can largely be attributed to the use of a smaller reference window size g_c. Selecting only large glaciers, often with a wider ablation zone, largely diminishes this discrepancy (fig. A.4), which supports our hypothesis. Thus, the employment of the Sentinel-2 satellites improved the resolution and therefore the analytical potential of the glacier centre flow line velocity data.

In the following sections of this chapter we will focus on median centre flow line surface velocities in the ablation zone (e.g. fig. 8a). For the sake of simplicity, we will refer to this as 'median velocity' if not explicitly stated otherwise. When we speak about the 'mean median velocity', we refer to the mean of median centre flow line surface velocity.

5.3 Terminus Type Variability in Velocity

Our analysis shows (fig. 8a) that the mean median velocity of lake-terminating glaciers (18.8 ±0.41 m/year) is substantially higher than the mean median velocity of land-termination glaciers (8.24 ±0.12 m/year)(table 5). Differences are negligible at the

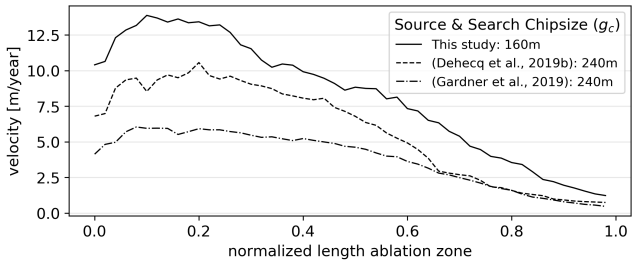

Figure 7: Regional median centre flow line surface velocity (m/year) comparison between Dehecq et al. (2019b) (dashed line), Gardner et al. (2019) (dashed-dotted line) and this study (solid line) of glacier greater than 3km^2 in area. All glaciers are normalized along their ablation length with the terminus positioned at the right end of this figure.

ELA, but become steadily larger throughout the ablation zone, with over the second half of the ablation zone a difference of 13.8 m/year (mean median velocity of 17.7 ±0.47 m/year for lake-terminating and 3.9 ±0.09 m/year for land-terminating glaciers)(table B.1). Land-terminating glaciers show a stagnant terminus with only little spread in the median velocity among the glacier population. In the contrary, the median velocity of lake-terminating glaciers decreases only slightly, but show a very large spread, indicating a large heterogeneity in lake-terminating dynamical behaviour. As expected from the uncertainty analysis, the overall coverage for lake-terminating glaciers is lower than for land-terminating glaciers (fig. 8b), but generally stays above 75% over the second half of the ablation zone.

A few of the median key characteristics of land- and lake-terminating glaciers are summarized in table 4. Overall, lake-terminating glaciers cover a larger surface area and show a slightly more negative mean surface slope over the ablation zone and might explain partially the overall contrast in the mean velocities (Bahr et al., 1997; Scherler et al., 2011a). However, this does not explain the large contrast in median velocity or heterogeneity at the glacier terminus. Interestingly, when only focusing on the second half of the ablation zone, where lake-land terminating median velocity contrast is greatest, the mean median surface slope of lake-terminating glaciers (-7.2 ±3.7) is lower than the slope of land-terminating glaciers (-8.2 ±4.54)(table B.1, suggesting that other factors than slope are responsible for the velocity contrast close to the glacier terminus.

5.3.1 Velocity Dependence on Orientation and Surface Area

In Chapter 2 we noted that glaciers flowing north onto the TP typically have larger accumulation zones and less debris cover compared to glaciers located in the Himalayan interior. Visual inspection of fig. 3 indicates that highest velocities are found at such localities, especially in Central West 1, Central 1 and East Himalaya, implying a positive correlation between glacier orientation and mean velocity. Concurrently, a large fraction of the total number of lake-terminating glaciers are orientated northwards, which might falsify the apparent relationship between surface velocity and terminus type proposed in previous section.

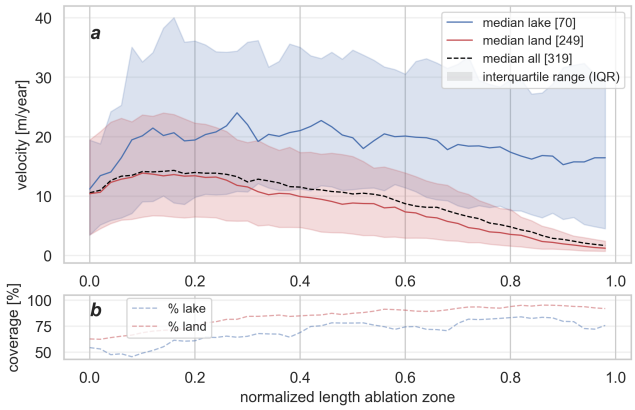

Figure 8: Median centre flow line surface velocity (m/year) (a) and coverage (%) of the velocity estimates (b). (a) The blue line represents the median of lake-terminating glacier, the red line the median of land-terminating glaciers and the black dashed line the whole glacier population. The spread among the glacier population is represented by the IQR, which is only shown around the lake-terminating and land-terminating median. The numbers at the legend indicate the population size.(b) The coverage is defined by the fraction of glaciers showing an uncertainty below 5m/year at a given position along the centre flow line.

Table 4: Several key characteristics for lake-terminating, land-terminating and all glaciers of this study. Upper and lower bounds represent one standard error (SE).

	Terminus Type		
Glacier Features	**Lake**	**Land**	**All**
ELA (m.a.s.l.)	5750 ±274 m.a.s.l.	5630 ±396	5670 ±373
Area (km^2)	7.48 ±4.92	6.40 ±4.11	6.68 ±4.42
Ablation Length (m)	3720 ±1602	3920 ±2017	3840 ±2017
Slope (degrees)	-8.8 ±4.1	-8.5 ±4.1	-8.6 ±4.1

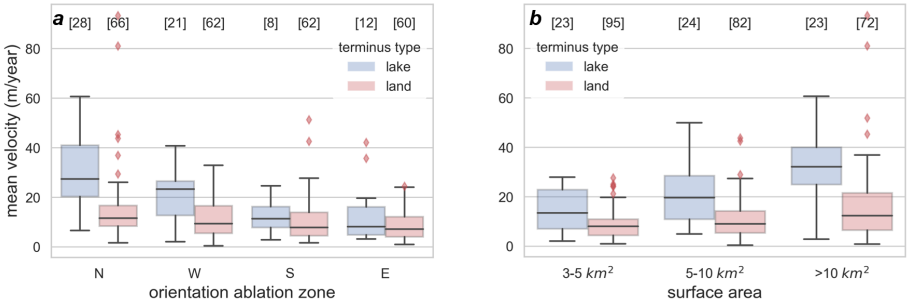

Figure 9: Boxplot showing the mean velocity contrast between lake-terminating glaciers (blue) and land-terminating glaciers (red) depending on the orientation of the ablation zone (a) and surface area (b). Boxes represent the IQR of the distribution, whereas points that are outside of the 3rd quartile plus 1.5 times the IQR range are plotted explicitly.

To investigate the link between the dynamics and orientation we therefore subdivide our dataset dependent on the orientation of the glacier ablation zone (fig. 9). The results show a large heterogeneity for lake-terminating glaciers, with highest velocities shown for glaciers with their ablation zone orientated to the north. Notwithstanding, for all orientations lake-terminating glaciers show a higher mean velocity than land-terminating glaciers, although contrast is only minor for glacier flowing east- or southwards. When only considering the second half of the ablation zone however, the lake-land terminating velocity contrast becomes substantial for all orientations (fig. B.1a).

We also analyse the role of glacier surface area onto mean glacier velocity. For this we separate the glaciers in three different glacier area bins such that the bins are of equal sample size. The results (fig. 9) show higher mean velocities for lake-terminating glaciers for each glacier area bin, with the largest contrast for glaciers greater than 10km^2. Note that in the largest size bin glacier are not bounded by an upper area limit, but nevertheless show a comparable median area of 19.2 $\pm$8.84 km^2 for lake-terminating glaciers and 18.70 $\pm$10.52 km^2 for land-terminating glaciers. Velocity outliers are particularly abundant at large (>10km^2) northward flowing land-terminating glaciers, such as the clean-ice Zeng Glacier in East Himalaya which shows a mean velocity of about 93m/year. Again, contrasting mean velocities between lake-terminating and land-terminating glaciers increase when solely considering the second half of the ablation zone (fig. B.1b), indicating that regardless of orientation and size, substantial contrast in glacier surface velocity is related to terminus type and increase towards the glacier tongue.

5.3.2 Regional Variability

To examine the regional variability in the lake-land contrasting surface velocities we subdivided the dataset depending on subregion (fig. 10). We find large differences in mean velocities between different regions, with highest mean velocities in Central West 1 (13.0 $\pm$0.40 m/year) and East Himalaya (13.1 $\pm$0.42 m/year) (table 5), areas with the largest proportions of clean ice. All regions show higher mean velocities for

Table 5: Mean of median regional centre flow line velocities of lake-terminating, land-terminating and all glaciers. Uncertainty estimates represent the 1 SE confidence interval.

	Terminus Type		
Himalaya Region	**Take Mean (m/year)**	**Land Mean (m/year)**	**Both Mean (m/year)**
Central West 1	20.0 ±1.57	13.1 ±0.40	13.0 ±0.40
Central 1	18.3 ±0.51	5.44 ±0.17	6.72 ±0.18
Central 2	11.8 ±2.49	6.03 ±0.23	6.56 ±0.21
Central East	18.2 ±1.47	8.89 ±0.34	10.2 ±0.32
East Himalaya	27.7 ±2.80	10.6 ±0.44	13.1 ±0.42
All	18.8 ±0.41	8.24 ±0.12	9.39 ±0.12

lake-terminating glacier than for land-terminating glaciers, though large variability between regions is apparent. In Central 2 mean velocity differences between lake-terminating (11.8 ±2.49 m/year) and land-terminating glaciers (6.03 ±0.23 m/year) are relatively modest, and coincides with a high proportion of debris-covered glaciers for both terminus types. For Central 1 and East Himalaya, a substantial part of the velocity contrast can be attributed to the relative high abundance of lakes at large clean-ice northward flowing glaciers onto the TP, explaining the large velocity contrast which is already substantial at the ELA. Finally, in the regions Central West 1 and Central 1 we observe an increase in velocity towards the terminus, indicating that a majority glaciers accelerate towards the glaciers-water interface. Trends in median velocity of lake terminating glaciers in these regions should the treated with cautiousness however, as the population of lake terminating glaciers is very limited (N=6,10). Nonetheless, all regions show a large contrast in heterogeneity close to the terminus, suggesting that the influence of proglacial lakes on glacier dynamics is a regional wide phenomenon.

5.4 Surface Cover on Glacier-Lake Dynamics

The regional subdivision in previous section revealed that regions with a high proportion of debris-covered glaciers, such as Central 2, coincide with relatively low surface velocities, and a lower contrast in velocity between lake-terminating and land-terminating glaciers. To examine the role of debris cover on glacier-lake dynamics, we subdivide our dataset into glaciers with a debris cover and clean-ice glaciers (fig. 11 a,c,e). Next to this, we compare the velocity dataset against the glacier surface elevation change dataset from King et al. (2019) (fig. 11 b,d,f), as amplified surface elevation changes data might hold valuable information on dynamic thinning. Also, since glacier surface elevation change is strongly controlled by the surface mass balance (Evatt et al., 2015; Vincent et al., 2016; Bisset et al., 2020) and hence reflect the control of surface cover on glacier dynamics (Benn et al., 2012; Dehecq et al., 2019a), it allows us to examine the contribution of debris cover onto glacier-lake dynamics.

The results show substantially higher velocities for lake-terminating glaciers, at both debris-covered and clean-ice glaciers (fig. 11c,e, table 6), although large differences depending on surface type are apparent. The overall mean velocities of debris-covered glaciers are generally lower (6.38 ±0.12) than clean-ice glaciers (12.1 ±0.18), and the contrast between mean velocities of debris-covered glaciers (11.5 ±0.63 vs 5.96

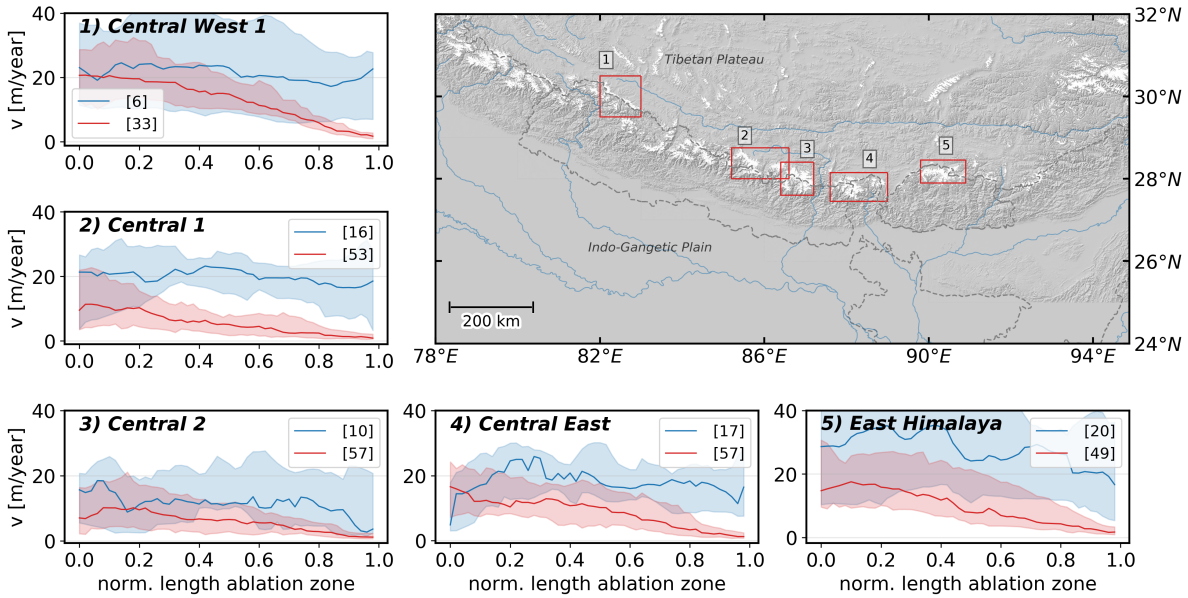

Figure 10: Subregional glacier median centre flow line velocity estimates and their location along the CE Himalaya (red rectangles). Blue lines and red lines represent lake-terminating glaciers and land-terminating glaciers respectively. The spread shows the IQR among the glacier population, with the number of glaciers shown in the legend between the brackets. This figure was generated using Matplotlib, vers. 3.1.2, together with Python, vers. 3.7.

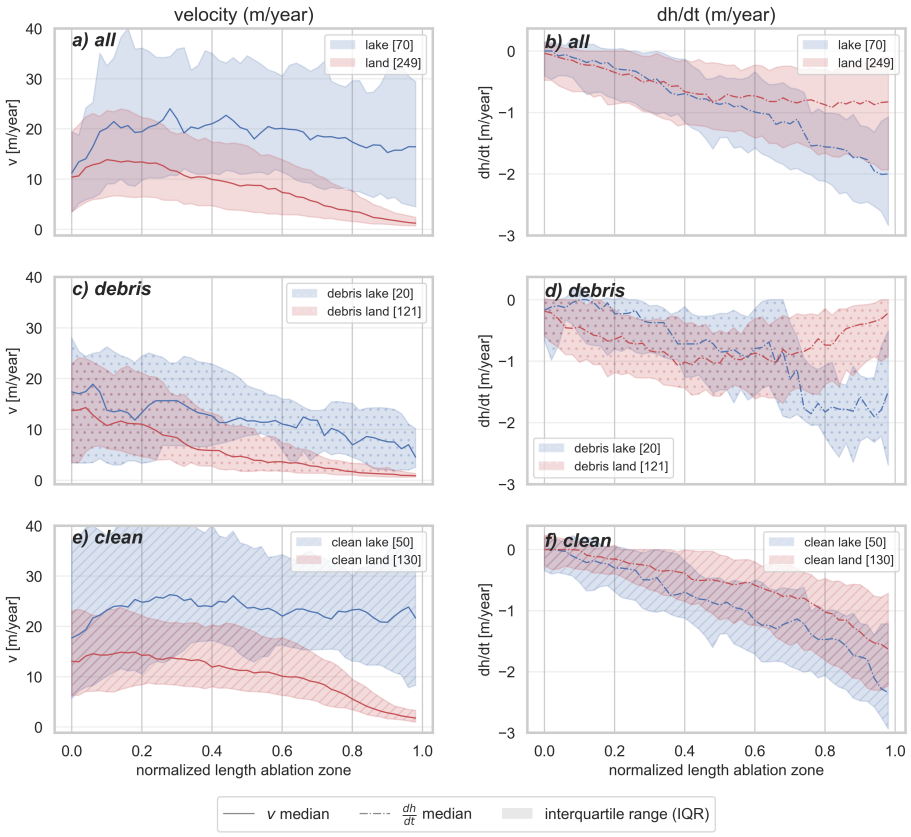

Figure 11: Glacier median centre flow line velocity (m/year) (a,c,e) and surface elevation change (dh/dt) estimates (after King et al. (2019))(b,d,e) for lake-terminating glaciers (blue) and land-terminating glaciers (red). A further subdivision is made between debris-covered glaciers (c,d) and clean-ice glaciers (e,f). The spread shows the IQR among the glacier population, with the number of glaciers shown in the legend between the brackets.

Table 6: Mean of median centre flow line velocities of lake-terminating, land-terminating and all glaciers, subdivided by surface cover. Uncertainty estimates represent the 1 SE confidence interval.

	Terminus Type		
Surface Cover	**Lake Mean (m/year)**	**Land Mean (m/year)**	**Both Mean (m/year)**
Clean	22.5 ±0.52	10.3 ±0.14	12.1 ±0.18
Debris	11.5 ±0.63	5.96 ±0.11	6.38 ±0.12
All	18.8 ±0.41	8.24 ±0.12	9.39 ±0.12

±0.11) is much smaller than at clean-ice ones (22.5 ±0.52 vs 10.3 ±0.14). For both debris-covered and clean-ice glaciers, higher velocities for lake-terminating glaciers overall coincide with elevated surface lowering, with largest contrasts found close to the terminus (fig. 11). Again however, large differences between debris-covered glaciers and clean-ice glacier exists, with most notably the concave-up profile of debris-covered land-terminating glaciers and the convex-down profile of clean-ice land-terminating glaciers.

In an effort to isolate the contribution of lakes on glacier dynamics, which will likely be sensitive to the type of surface cover (Benn et al., 2012), the impact of debris cover on land-terminating glaciers has to be understood. Land-terminating debris-covered glaciers very quickly become close to stagnant, resulting in a concave-down velocity profile (fig. 11c). This concave-down profile coincides with a clear concave-up surface elevation change profile in the ablation zone (fig. 11d), with halfway the highest surface lowering rates of about 1 m/year. Intrinsically, a concave-down velocity profile shows greatest positive emergence velocities at a relative upstream position along the ablation zone. This indicates that the surface mass balance (SMB), which is the sum of elevation change and emergence velocity, shows a gradient that is at least as reversed as concave-up profile, with ablation rates that are the greatest at central and upper reaches of the ablation zone. This result is in line with the inferred concave-up SMB gradients on debris-covered glaciers from Bisset et al. (2020), and with both observational based and model based studies on the Langtang Glacier in Nepal (Steiner et al., 2019; Wijngaard et al., 2019). Clearly, the thick layer of debris close to the terminus offsets the effects of higher air temperatures at lower elevations, resulting in mass loss that is therefore focused in the mid parts of glacier ablation zones, causing localised surface lowering. This results in a reduction in down glacier surface gradient, which is manifested by the large contrast in surface slope in the second half of the ablation zone between debris covered and clean glaciers (-5.5 ±2.4° vs -10.8 ±3.7°). The reduced surface gradient in turn reduce driving stress and glacier velocity, resulting in the largely stagnant lower ablation zones of the debris covered glaciers, and closely agrees with with the conceptual model on the evolution of debris-covered glaciers under transient atmospheric warming from Benn et al. (2012).

Lake-terminating debris-covered glaciers do not follow this concave-down velocity profile, show roughly a linear decrease in velocity but never become stagnant, and shows close to the terminus a larger spread than their. Also, lake-terminating glaciers show a distinct enhanced surface lowering around the last quarter of their ablation length, with rates of surface lowering exceeding rates anywhere found along the ablation length of land terminating glaciers. Notably, these lake terminating glaciers are generally smaller in surface area (6.78 ±4.4 km^2 vs 9.4 ±6.9 km^2) and the ablation

length much shorter (2720 ±1660 m vs 5680 ±3084 m), and rough visual estimation off pro-glacial lake dimensions shows that lake lengths often vary between 1 and 4km in length, which might make up for most of the discrepancy in debris covered glacier length between terminus type. Arguably, the length that lake terminating glaciers retreated should be accounted for in the analysis, which would reduce the median lake-land velocity contrast drastically.

Land-terminating clean-ice glaciers show an dynamically active flow (where v>5 m/year) for the majority of its ablation zone, characterized with a convex-down profile. Surface elevation change rates become increasingly more negative towards the terminus (fig. 11f), which indicates that glacier mass loss is largely controlled by ambient temperature change. The resulting sustained surface gradient ensures an active flow along the largest parts of the ablation zone. In fact, the convex-down velocity profile reveals a significantly more negative SMB at the terminus than for debris covered glaciers, which is party compensated for by the positive emergence velocities at the terminus of land-terminating clean-ice glaciers.

For lake-terminating clean-ice glaciers, velocity remains close to constant towards the terminus and shows a very large spread among the glacier population (fig. 11e). Enhanced surface lowering at lake-terminating clean-ice glaciers steadily grows to -0.5m/year towards the terminus and is less pronounced than the surface lowering contrast at debris-covered glaciers. We find no substantial differences in altidudinal distribution between lake-terminating and land-terminating glaciers are observed that could partly explain this offset. For clean-ice glaciers, the large velocity contrast coincides with a larger surface area of lake-terminating glaciers compared to land-terminating glaciers (8.4 ±6.2 km^2 vs 4.7 ±2.0 km^2), and a longer ablation length of lake-terminating glaciers (3800 ±1601m) compared to land-terminating glaciers (3040 ±1127m).

Where clean-ice lake-terminating glaciers are greater in area size and show a longer ablation zone than clean-ice land-terminating glaciers, debris-cover lake-terminating glaciers are generally much smaller and show a shorter ablation zone. This contrast in glacier dimensions illustrates an important control surface cover has on lake-land terminating dynamics, which is related to the morphological settings in which proglacial lakes are prone to develop. Clean-ice land-terminating glaciers have shown large retreat rates over the past decades (Bolch et al., 2008; Basnett et al., 2013), and only the glaciers with extensive accumulation zones, often flowing onto the TP, possessed enough erosion potential to form an extensive Little Ice Age (LIA) moraines terminal moraine (Scherler et al., 2011a). Overdeepening at glaciers flowing onto the TP plateau is not only promoted by terminal moraines but is a inherent feature of the reversed lope of the TP itself (Royden et al., 2008), making these localities a hot spot of pro-glacial lake development. Therefore, clean-ice lake-terminating glaciers are often large, and show consequently higher velocities than their land-terminating counterpart.

Unlike for clean-ice glaciers, our results suggest that there is no clear preference for proglacial lake development to glacier area size. This situation drastically changes once a proglacial lake develops, a transformation which is associated with a drastic increase in retreat rates (Basnett et al., 2013; King et al., 2019; Watson et al., 2020), and results in lake-terminating glaciers of shorter length than their land-terminating counterpart. Thus, lake-terminating debris-covered glaciers can evolve from the 'median' land-terminating glacier population, whereas lake-terminating clean-ice glaciers predominantly evolve from land-terminating glaciers that are relatively great in surface area. This, together with the over-representation of clean-ice glaciers in the

lake-terminating glacier population (50 out of 70), explains a large part of the median lake-land velocity contrast (fig. 11a). Also this over-representation of clean-ice glaciers in the lake terminating glacier population explains a significant part of the contrasting thinning observed in fig. 11b, which makes it erroneous to attribute this contrast entirely to dynamic thinning.

Notwithstanding, the large spread at the terminus of lake-terminating glaciers, with accelerating velocity for almost half of the population, and elevated surface lowering for both debris-covered and clean-ice lake-terminating glaciers clearly shows that dynamic thinning is a process that has to be considered. We relate the lower spread at the terminus of lake-terminating debris-covered glaciers to a lower driving force which is apparent at the ablation zone of debris-covered glaciers. A low driving force limits the potential of terminus acceleration onto a proglacial lake induced reduction of resisting forces, hence we argue that the impact of proglacial lakes on the velocity of proglacial lakes is existent, but only limited compared to clean-ice glaciers. Defining an up-glacier extent to which the dynamic impact is confined is troublesome as this might highly vary among the glacier population and asks for a detailed isolation of proglacial lake related dynamical drivers. A very rough estimation based on the location of divergence of decelerating and accelerating glaciers (fig. B.2) would suggest that most of the dynamic impact is confined to one kilometer reach from the terminus.

5.5 Supraglacial Lakes on Glacier Surface Lowering

Benn et al. (2012) noted that supraglacial lakes, which can be either be sustained by a local perched water table or by a moraine dam, show ablation rates that are typically one or two orders of magnitude greater than sub-debris melt rates. To examine the control of supraglacial lakes on surface lowering, we subdivide our dataset of debris-covered glaciers in land-terminating glaciers, glaciers with supraglacial lakes and lake-terminating glaciers. The results show that glaciers with supraglacial lakes have an overall similar concave-down velocity and concave-up surface lowering profile compared to land-terminating debris-covered glaciers (fig. 12), and never reaches the surface lowering rates observed at lake-terminating glaciers. Compared to land-terminating glaciers mean surface slope at the ablation zone is lower (-5.1 $\pm$2.1 vs -5.5 $\pm$2.4) and surface velocities become even quicker close to stagnant. Noteworthy, most supraglacial lakes are located close to the terminus, where surface lowering is only modest, indicating that their effect on mass loss is only limited compared to the more seasonal and unstable supra-glacial ponds generally found more up-glacier (Steiner et al., 2019). The greater surface lowering of lake-terminating glaciers can therefore not be explained by the presence of these supra-glacial lakes, and indicates that these elevated lowering rates are likely to be attributed to dynamic thinning.

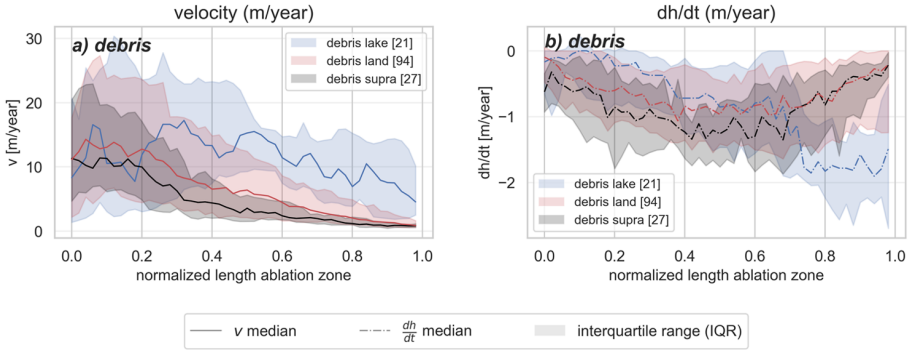

Figure 12: Glacier median centre flow line velocity (m/year) (a) and surface elevation change (dh/dt) estimates (after King et al. (2019))(b) for debris-covered lake-terminating glaciers (blue) land-terminating glaciers (red) and glaciers with supraglacial lakes (black). The spread among the glacier population is represented by the IQR. The numbers between brackets at the legend indicate the population size.

6 Discussion

6.1 Limitations of our Analysis

In this study we compared our surface velocity dataset with an effective data at 08-2018 to a surface elevation change dataset with an effective data around mid-2015, which means that the datasets are separated by about three years. With average retreat rates 26.8 ± 1.4 m/year for lake-terminating glaciers reported by King et al. (2019), this would result in a failure to capture on average the last 100m of elevation change at the terminus. As our results showed that surface lowering increases towards the terminus, this implies a loss of valuable surface elevation change data. Actually, the amount of thinning we missed might be disproportionately large as we expect that areas with great dynamic thinning rates coincide with high retreat rates through the development of extensive transverse crevasses (Benn et al., 2007a). Future analysis should overcome this limitation by creating datasets with an effective date that is virtually aligned.

Our choice to analyse the centreline data along the normalized length of the ablation zone gives us great insight into the dynamic influence of terminus type and surface cover, but limits us to rule out the effect of climate on surface elevation change. This also limits the possibility to properly attribute contrasting surface elevation change rates of lake-terminating and land-termination glaciers to dynamic thinning, which is especially true for clean-ice glaciers whose thinning rates appear to be highly dependent on climate hence elevation. Analysing the data by binning the glacier surface by elevation bands, as done by King et al. (2019); Maurer et al. (2019) and Brun et al. (2019) circumvents this problem at subregional scales, but also results in a loss off valuable information of glacier behaviour, especially on dynamics at the terminus.

Also, the analysis of median centre flow line data largely limits this study to a qualitative kind and makes it impossible to extrapolate the data to entire glacierized region. This limitation can only be circumvented when firstly, very high resolution data that can resolve areas with high shear becomes widely available, and secondly, the relation between surface velocity and mean ice velocity become much better parameterized, which is highly dependent on the adoption of basal sliding law (Truffer, 2004; Schoof, 2005; Egholm et al., 2011). Only then, a proper total budget on glacier dynamics is possible, though this might be very ambiguous. Related to this, our analysis is focused on glaciers which are greater in area than 3km^2, and make our observations skewed towards higher velocities. We foresee this bias not to be of great importance as larger glaciers occupy a dominant proportion of the total Himalayan glacier surface area (fig. 2) and hence are of largest relevance to mass loss contributions.

Another limitation is the diagnostic nature of our study, with no information on the temporal evolution of the dynamic behaviour onto the development of a lake. As our results showed, comparing land terminating glaciers to lake terminating glaciers is highly insightful but also partly misleading, as many land-terminating glaciers vary from lake-terminating glaciers not only as a stage in their glacier evolution, but also in nature. For example, we showed that this imposed difficulties for the interpretation of the lake-land velocity contrast of clean-ice glaciers. Retrieving a temporal dataset is for now only possible for relatively wide glaciers, such as done by Liu et al. (2020), as our analysis showed that Landsat-8 imagery not yet perfectly resolves the glacier centre flow line velocity when glaciers are too small.

6.2 Lake-Terminating Heterogeneity and Possible Drivers of Dynamic Thinning

Our results show that the contrasting dynamical behaviour between lake-terminating glaciers and land-terminating glaciers is at least partially to be attributed to dynamic thinning and is likely limited to within the last kilometer of the ablation zone. However, the substantial spread at the terminus within the lake-terminating population makes it evident (figure 11a) that there are factors controlling dynamic thinning rates beyond the median quantities such as glacier area, length and slope that this study covered so far.

Alpine lake-terminating glaciers critically differ from marine-terminating glaciers in that proglacial lake development is already a process by itself, with plenty of glaciers that are developing, or yet have to develop a proglacial lake. In the early stages of lake development, the impact of the lake on the glacier might be limited to direct frontal processes such as subaqueous melting or calving through undercutting (e.g. Benn et al., 2007b), with only limited reduction of effective pressure at the glacial bed. In these situations the dynamical behaviour is unlikely to be altered.

When a proglacial lake further develops and deepens, effective pressure at the glacier bed becomes further reduces and the terminus might even reach flotation, and eventually reduce basal drag enough to initiate an acceleration accompanied by dynamical thinning. In such a transition glacier might enter a self-reinforcing calving cycle (Benn et al., 2007a), where the longitudinal velocity gradient progressively weakens the ice front by the opening of transverse crevasses, initiating rapid calving retreat and moving the glacier terminus to more buoyant deeper waters. Transverse crevasses close to the terminus therefore gives us indirect indications of dynamic thinning, and plenty of clean-ice glaciers show this observational evidence (fig. 13a,c,d). For heavily debris-covered glaciers however, crevasses might often be well hidden under the thick pile of debris, making this analysis virtually impossible (fig. **??**b). Indeed, Liu et al. (2020) found at the Longbasaba Glacier in Central East Himalaya a remarkable acceleration of the lake-terminating terminus since 2012, and this coincided with above-average retreat rates, implying a positive feedback on glacier retreat through dynamical thinning. Direct evidence for Himalayan glaciers reaching flotation is difficult however, for obvious reasons, and to our knowledge still absent in the Himalaya. Notably, the dynamic thinning at many glaciers might often be very subtle, for example at heavily debris-covered glaciers, though can play an essential role in this positive feedback by weakening the ice though opening crevasses or a further reduction of effective pressure, and initiating rapid retreat.

Also the role of lateral drag certainly cannot be neglected and is important in settings with a variable basin width (Benn et al., 2007b). For example, many lake terminating glaciers have their terminus positioned at local widening of the glacier basin, and therefore suggest that the relative increase of lateral drag act as local stabilizing points of glacier terminus. However, such localities often coincide with shallower lake depths, which complicates the evaluation of the relative importance of lateral drag and basal drag in the force balance. At last, Benn et al. (2007b) noted that longitudinal stress gradient might be of high importance in setting that rapid change, something not uncommon in valley glacier settings. For example, clear transverse crevasses in fig. 13d indicate, although the glacier seemingly moved to shallower waters, that the glacier is adjusting to the imposed force imbalance through the removal of frontal ice. Explicitly resolving the contribution of the longitudinal stress gradient is a challenging task however, as it considerably increases the complexity

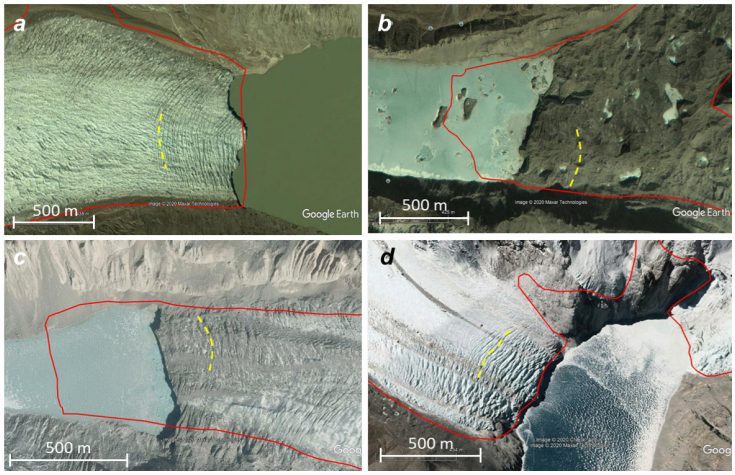

Figure 13: Impression of the distribution of transverse crevasses among the lake-terminating glacier population in the Himalayan region, with the dashed yellow lines indicating the orientation of the crevasses. Glaciers RGI60-15.10994 and RGI60-15.02591 (a,c) are (almost) clean-ice glaciers with a clear crevassed zone, whereas glacier RGI60-15.03743 (b) is covered by a thick mantle of debris, though several transverse crevasses are visible. (d) The Guoluo Glacier (RGI60-15.02591) shows a clear crevassed zone, although seems to have retreated to shallow parts of the lake.

of a glacier model.

6.3 Implications for Future Evolution of Himalayan Glaciers

As King et al. (2019) pointed out, regional ice loss through lake-terminating dynamics will remain important in the near future, given the sustained expansion of proglacial lakes across the Himalayan region (Nie et al., 2017; Zhang et al., 2015) and the susceptibility of many debris-covered glaciers for proglacial lake development. However, the overdeepening at many large clean-ice land-terminating glaciers should also not be underestimated (Linsbauer et al., 2016) and their future contribution to regional ice loss might be disproportionately large, considering the region wide active flow and the substantial dynamic thinning at their lake-terminating counterparts. Many of these clean-ice glaciers drain northwards into the tributaries of the Brahmaputra river, and changes in melt water projections are of essential importance for millions of people in downstream regions (Immerzeel et al., 2010).

In order to better understand the impact of proglacial lakes onto glacier dynamics and to find out whether the contribution of lake-terminating glaciers to Himalayan ice mass loss may increase further, more multi-decadal analysis on the glacier-lake dynamics, such as done by Liu et al. (2020), is needed. Also there is an urgent call for more modeling studies on glacier-lake dynamics like Tsutaki et al. (2019) and such studies should address problems of varying complexity such as glacier flow responds onto a reduction of effective pressure or changes in basin width, or higher-order models addressing the importance of the longitudinal stress gradient. Ultimately, comprehensive transient models are needed that couple lake development, glacier dynamics and calving fluxes to make better predictions of near future ice loss of Himalaya glaciers.

7 Conclusions

In this study, we documented the instantaneous 2017-2019 surface velocity in the ablation zone of glaciers larger than 3km^2 by employing the Sentinel-2 optical satellite imagery at five proglacial lake-prevalent subregions in the Himalayan mountains. All suitable November image pairs we selected and matched in Fourier Space using a method called 'Orientation Correlation', providing a detailed and spatially complete picture of glacier flow. Our results show that the enhanced resolution of Sentinel-2 with respect to Landsat-8 (10m vs 15m) enabled the image-matching algorithm to better resolve the velocity field at small glaciers, and thereby improving the potential for the analysis on glacier centre flow line velocities.

Analysis of the centre flow line velocity profiles revealed that lake-terminating glaciers display substantially higher flow velocities than land-terminating glaciers (18.8 $\pm$0.41 m/year vs 8.24 $\pm$0.12 m/year), and that this finding is consistent regardless the orientation, glacier size and subregion of the glacier population. The velocity contrast between lake-terminating and land-terminating clean-ice glaciers is much greater than for debris-covered glaciers, and we show a major contribution of the mean velocity difference can be attributed to the overrepresentation of large clean-ice glaciers in the lake-terminating population.

Notwithstanding, both clean-ice and debris-covered lake-terminating glaciers show large heterogeneous behaviour at the glacier terminus, remain dynamically active along the entire flow and show an accelerating for almost half of the glacier population, revealing that dynamic thinning is a process that is prevalent in the Himalayan region. We relate the lower spread in terminus behaviour of lake-terminating debris-covered glaciers to the reduced driving stress compared their clean-ice counterparts.

A quantitative attribution of surface flow acceleration to dynamic thinning rates, concealed in the elevation change dataset from King et al. (2019), is yet problematic because of the large heterogeneity in glacier behaviour, specific choices regarding our analysis and temporal discrepancies between the two datasets. Nevertheless, a positive correlation between high terminal velocities and elevated surface lowering is evident for both surface types, indicating that future analysis could better resolve this relation.

The large heterogeneity at the terminus of lake-terminating glaciers is likely related to the wide variety of settings in which the glaciers can be found, resulting in a highly variable contribution of basal drag, lateral drag or longitudinal stress gradient. The contribution of ice mass loss from lake-terminating glaciers is unlikely to diminish in the near future, but the exact contribution to melt water supply in the next decades is still highly uncertain. Improved understanding of lake-terminating glacier dynamics is therefore imperative for the future of those people that depend on a year-round water supply from the Brahmaputra river.

References

Ageta, Y. and Higuchi, K. (1984). Estimation of mass balance components of a summer-accumulation type glacier in the Nepal Himalaya. *Geografiska Annaler, Series A*, 66 A(3):249–255.

Altena, B., Haga, O. N., Nuth, C., and Kääb, A. (2019). Monitoring sub-weekly evolution of surface velocity and elevation for a high-latitude surging glacier using sentinel-2. In *International Archives of the Photogrammetry, Remote Sensing and Spatial Information Sciences - ISPRS Archives*, volume 42, pages 1723–1727.

Anderson, L. S. and Anderson, R. S. (2016). Modeling debris-covered glaciers: response to steady debris deposition. *The Cryosphere*, 10(3):1105–1124.

Bahr, D. B., Meier, M. F., and Peckham, S. D. (1997). The physical basis of glacier volume-area scaling. *Journal of Geophysical Research: Solid Earth*, 102(B9):20355–20362.

Basnett, S., Kulkarni, A. V., and Bolch, T. (2013). The influence of debris cover and glacial lakes on the recession of glaciers in Sikkim Himalaya, India. *Journal of Glaciology*, 59(218):1035–1046.

Benn, D. I., Bolch, T., Hands, K., Gulley, J., Luckman, A., Nicholson, L. I., Quincey, D., Thompson, S., Toumi, R., and Wiseman, S. (2012). Response of debris-covered glaciers in the Mount Everest region to recent warming, and implications for outburst flood hazards.

Benn, D. I., Hulton, N. R., and Mottram, R. H. (2007a). 'Calving laws', 'sliding laws' and the stability of tidewater glaciers. In *Annals of Glaciology*, volume 46, pages 123–130.

Benn, D. I. and Lehmkuhl, F. (2000). Mass balance and equilibrium-line altitudes of glaciers in high-mountain environments. In *Quaternary International*, volume 65-66, pages 15–29. Pergamon.

Benn, D. I., Warren, C. R., and Mottram, R. H. (2007b). Calving processes and the dynamics of calving glaciers. *Earth-Science Reviews*, 82(3-4):143–179.

Bhambri, R., Watson, C. S., Hewitt, K., Haritashya, U. K., Kargel, J. S., Pratap Shahi, A., Chand, P., Kumar, A., Verma, A., and Govil, H. (2020). The hazardous 2017–2019 surge and river damming by Shispare Glacier, Karakoram. *Scientific Reports*, 10(1):1–14.

Bindschadler, R. A. and Scambos, T. A. (1991). Satellite-image-derived velocity field of an Antarctic ice stream. *Science*, 252(5003):242–246.

Bisset, R. R., Dehecq, A., Goldberg, D. N., Huss, M., Bingham, R. G., and Gourmelen, N. (2020). Reversed surface-mass-balance gradients on himalayan debris-covered glaciers inferred from remote sensing. *Remote Sensing*, 12(10):1563.

Bolch, T., Buchroithner, M., Pieczonka, T., and Kunert, A. (2008). Planimetric and volumetric glacier changes in the Khumbu Himal, Nepal, since 1962 using Corona, Landsat TM and ASTER data. *Journal of Glaciology*, 54(187):592–600.

Bolch, T., Kulkarni, A., Kääb, A., Huggel, C., Paul, F., Cogley, J. G., Frey, H., Kargel, J. S., Fujita, K., Scheel, M., Bajracharya, S., and Stoffel, M. (2012). The state and fate of himalayan glaciers.

Bookhagen, B. and Burbank, D. W. (2010). Toward a complete Himalayan hydrological budget: Spatiotemporal distribution of snowmelt and rainfall and their impact on river discharge. *Journal of Geophysical Research: Earth Surface*, 115(3).

Braithwaite, R. J. and Raper, S. C. (2009). Estimating equilibrium-line altitude (ELA) from glacier inventory data. *Annals of Glaciology*, 50(53):127–132.

Brun, F., Berthier, E., Wagnon, P., Kääb, A., and Treichler, D. (2017). A spatially resolved estimate of High Mountain Asia glacier mass balances from 2000 to 2016. *Nature Geoscience*, 10(9):668–673.

Brun, F., Buri, P., Miles, E. S., Wagnon, P., Steiner, J., Berthier, E., Ragettli, S., Kraaijenbrink, P., Immerzeel, W. W., and Pellicciotti, F. (2016). Quantifying volume loss from ice cliffs on debris-covered glaciers using high-resolution terrestrial and aerial photogrammetry. *Journal of Glaciology*, 62(234):684–695.

Brun, F., Wagnon, P., Berthier, E., Jomelli, V., Maharjan, S. B., Shrestha, F., and Kraaijenbrink, P. D. (2019). Heterogeneous Influence of Glacier Morphology on the Mass Balance Variability in High Mountain Asia. *Journal of Geophysical Research: Earth Surface*, 124(6):1331–1345.

Brun, F., Wagnon, P., Berthier, E., Shea, J. M., Immerzeel, W. W., Kraaijenbrink, P. D., Vincent, C., Reverchon, C., Shrestha, D., and Arnaud, Y. (2018). Ice cliff contribution to the tongue-wide ablation of Changri Nup Glacier, Nepal, central Himalaya. *Cryosphere*, 12(11):3439–3457.

Burgess, E. W., Forster, R. R., and Larsen, C. F. (2013). Flow velocities of Alaskan glaciers. *Nature Communications*, 4(1):1–8.

Carrivick, J. L. and Tweed, F. S. (2016). A global assessment of the societal impacts of glacier outburst floods. *Global and Planetary Change*, 144:1–16.

Chu, J. T. and Hotelling, H. (1955). The Moments of the Sample Median. *Annals of Mathematical Statistics*, 26(4):593–606.

Clerc, S. (2020). Sentinel-2 L1C data quality report. Technical report.

Dehecq, A., Gourmelen, N., Gardner, A. S., Brun, F., Goldberg, D., Nienow, P. W., Berthier, E., Vincent, C., Wagnon, P., and Trouvé, E. (2019a). Twenty-first century glacier slowdown driven by mass loss in High Mountain Asia. *Nature Geoscience*, 12(1):22–27.

Dehecq, A., Gourmelen, N., and Trouve, E. (2015). Deriving large-scale glacier velocities from a complete satellite archive: Application to the Pamir-Karakoram-Himalaya. *Remote Sensing of Environment*, 162:55–66.

Dehecq, A., Gourmelen, N., and Trouvé, E. (2019b). High Mountain Asia glacier velocities 2013-2015 (Landsat 8).

Drusch, M., Del Bello, U., Carlier, S., Colin, O., Fernandez, V., Gascon, F., Hoersch, B., Isola, C., Laberinti, P., Martimort, P., Meygret, A., Spoto, F., Sy, O., Marchese, F., and Bargellini, P. (2012). Sentinel-2: ESA's Optical High-Resolution Mission for GMES Operational Services. *Remote Sensing of Environment*, 120:25–36.

Egholm, D. L., Knudsen, M. F., Clark, C. D., and Lesemann, J. E. (2011). Modeling the flow of glaciers in steep terrains: The integrated second-order shallow ice approximation (iSOSIA). *Journal of Geophysical Research: Earth Surface*, 116(2).

Evatt, G. W., Abrahams, I. D., Heil, M., Mayer, C., Kingslake, J., Mitchell, S. L., Fowler, A. C., and Clark, C. D. (2015). Glacial melt under a porous debris layer. In *Journal of Glaciology*, volume 61, pages 825–836.

Fitch, A., Kadyrov, A., Christmas, W., and Kittler, J. (2002). Orientation Correlation. In *IN BRITISH MACHINE VISION CONFERENCE*, pages 1–11.

Gardelle, J., Arnaud, Y., and Berthier, E. (2011). Contrasted evolution of glacial lakes along the Hindu Kush Himalaya mountain range between 1990 and 2009. *Global and Planetary Change*, 75(1-2):47–55.

Gardelle, J., Berthier, E., Arnaud, Y., and Kääb, A. (2013). Region-wide glacier mass balances over the Pamir-Karakoram-Himalaya during 1999–2011. *Cryosphere*, 7(4):1263–1286.

Gardner, A., Lei, Y., and Agram, P. (2020). autoRIFT (autonomous Repeat Image Feature Tracking).

Gardner, A. S., Fahnestock, M. A., and Scambos, T. A. (2019). ITS_LIVE Regional Glacier and Ice Sheet Surface Velocities. Data archived at National Snow and Ice Data Center.

Guizar-Sicairos, M., Thurman, S. T., and Fienup, J. R. (2008). Efficient subpixel image registration algorithms. *Optics Letters*, 33(2):156.

Harrison, W. D., Echelmeyer, K. A., Cosgrove, D. M., and Raymond, C. F. (1992). The determination of glacier speed by time-lapse photography under unfavorable conditions. *Journal of Glaciology*, 38(129):257–265.

Heid, T. and Kääb, A. (2012). Evaluation of existing image matching methods for deriving glacier surface displacements globally from optical satellite imagery. *Remote Sensing of Environment*, 118:339–355.

Immerzeel, W. W., Kraaijenbrink, P. D., Shea, J. M., Shrestha, A. B., Pellicciotti, F., Bierkens, M. F., and De Jong, S. M. (2014). High-resolution monitoring of Himalayan glacier dynamics using unmanned aerial vehicles. *Remote Sensing of Environment*, 150:93–103.

Immerzeel, W. W., Van Beek, L. P., and Bierkens, M. F. (2010). Climate change will affect the asian water towers. *Science*, 328(5984):1382–1385.

Kääb, A., Berthier, E., Nuth, C., Gardelle, J., and Arnaud, Y. (2012). Contrasting patterns of early twenty-first-century glacier mass change in the Himalayas. *Nature*, 488(7412):495–498.

Kääb, A., Winsvold, S. H., Altena, B., Nuth, C., Nagler, T., and Wuite, J. (2016). Glacier remote sensing using sentinel-2. part I: Radiometric and geometric performance, and application to ice velocity. *Remote Sensing*, 8(7):598.

Kienholz, C., Rich, J. L., Arendt, A. A., and Hock, R. (2014). A new method for deriving glacier centerlines applied to glaciers in Alaska and northwest Canada. *Cryosphere*, 8(2):503–519.

King, O., Bhattacharya, A., Bhambri, R., and Bolch, T. (2019). Glacial lakes exacerbate Himalayan glacier mass loss. *Scientific Reports*, 9(1).

King, O., Dehecq, A., Quincey, D., and Carrivick, J. (2018). Contrasting geometric and dynamic evolution of lake and land-terminating glaciers in the central Himalaya. *Global and Planetary Change*, 167:46–60.

King, O., Quincey, D. J., Carrivick, J. L., and Rowan, A. V. (2017). Spatial variability in mass loss of glaciers in the everest region, central Himalayas, between 2000 and 2015. *Cryosphere*, 11(1):407–426.

Kirkbride, M. P. and Warren, C. R. (1999). Tasman Glacier, New Zealand: 20th-century thinning and predicted calving retreat. *Global and Planetary Change*, 22(1-4):11–28.

Krimmel, R. M. and Vaughn, B. H. (1987). Columbia Glacier, Alaska: changes in velocity 1977-1986. *Journal of Geophysical Research*, 92(B9):8961–8968.

Leys, C., Ley, C., Klein, O., Bernard, P., and Licata, L. (2013). Detecting outliers: Do not use standard deviation around the mean, use absolute deviation around the median. *Journal of Experimental Social Psychology*, 49(4):764–766.

Linsbauer, A., Frey, H., Haeberli, W., Machguth, H., Azam, M. F., and Allen, S. (2016). Modelling glacier-bed overdeepenings and possible future lakes for the glaciers in the Himalaya-Karakoram region. *Annals of Glaciology*, 57(71):119–130.

Liu, Q., Mayer, C., Wang, X., Nie, Y., Wu, K., Wei, J., and Liu, S. (2020). Interannual flow dynamics driven by frontal retreat of a lake-terminating glacier in the Chinese Central Himalaya. *Earth and Planetary Science Letters*, 546:116450.

Lutz, A. F., Immerzeel, W. W., Gobiet, A., Pellicciotti, F., and Bierkens, M. F. (2013). Comparison of climate change signals in CMIP3 and CMIP5 multi-model ensembles and implications for Central Asian glaciers. *Hydrology and Earth System Sciences*, 17(9):3661–3677.

Maurer, J. M., Schaefer, J. M., Rupper, S., and Corley, A. (2019). Acceleration of ice loss across the Himalayas over the past 40 years. *Science Advances*, 5(6).

Maussion, F., Butenko, A., Champollion, N., Dusch, M., Eis, J., Fourteau, K., Gregor, P., Jarosch, A. H., Landmann, J., Oesterle, F., Recinos, B., Rothenpieler, T., Vlug, A., Wild, C. T., and Marzeion, B. (2019). The Open Global Glacier Model (OGGM) v1.1. *Geoscientific Model Development*, 12(3):909–931.

McClellan, J. H., Schafer, R. W., and Yoder, M. A. (1999). *Digital signal processing first*, volume 16. Pearson/Prentice Hall.

Miles, E. S., Pellicciotti, F., Willis, I. C., Steiner, J. F., Buri, P., and Arnold, N. S. (2016). Refined energy-balance modelling of a supraglacial pond, Langtang Khola, Nepal. *Annals of Glaciology*, 57(71):29–40.

Nagler, T., Rott, H., Hetzenecker, M., Wuite, J., and Potin, P. (2015). The Sentinel-1 mission: New opportunities for ice sheet observations. *Remote Sensing*, 7(7):9371–9389.

Nagy, T. and Andreassen, L. M. (2019). Glacier surface velocity mapping with Sentinel-2 imagery in Norway. Technical Report 37.

Nie, Y., Sheng, Y., Liu, Q., Liu, L., Liu, S., Zhang, Y., and Song, C. (2017). A regional-scale assessment of Himalayan glacial lake changes using satellite observations from 1990 to 2015. *Remote Sensing of Environment*, 189:1–13.

Pellicciotti, F., Stephan, C., Miles, E., Herreid, S., Immerzeel, W. W., and Bolch, T. (2015). Mass-balance changes of the debris-covered glaciers in the Langtang Himal, Nepal, from 1974 to 1999. *Journal of Glaciology*, 61(226):373–386.

Quincey, D. J., Luckman, A., and Benn, D. (2009). Quantification of Everest region glacier velocities between 1992 and 2002, using satellite radar interferometry and feature tracking. *Journal of Glaciology*, 55(192):596–606.

Quincey, D. J., Richardson, S. D., Luckman, A., Lucas, R. M., Reynolds, J. M., Hambrey, M. J., and Glasser, N. F. (2007). Early recognition of glacial lake hazards in the Himalaya using remote sensing datasets. *Global and Planetary Change*, 56(1-2):137–152.

Richardson, S. D. and Reynolds, J. M. (2000). An overview of glacial hazards in the Himalayas. In *Quaternary International*, volume 65-66, pages 31–47. Pergamon.

Rounce, D. R., Quincey, D. J., and McKinney, D. C. (2015). Debris-covered glacier energy balance model for Imja-Lhotse Shar Glacier in the Everest region of Nepal. *Cryosphere*, 9(6):2295–2310.

Royden, L. H., Burchfiel, B. C., and Van Der Hilst, R. D. (2008). The geological evolution of the Tibetan plateau.

Sakai, A., Nishimura, K., Kadota, T., and Takeuchi, N. (2009). Onset of calving at supraglacial lakes on debris-covered glaciers of the Nepal Himalaya. *Journal of Glaciology*, 55(193):909–917.

Salerno, F., Thakuri, S., Tartari, G., Nuimura, T., Sunako, S., Sakai, A., and Fujita, K. (2017). Debris-covered glacier anomaly? Morphological factors controlling changes in the mass balance, surface area, terminus position, and snow line altitude of Himalayan glaciers. *Earth and Planetary Science Letters*, 471:19–31.

Scherler, D., Bookhagen, B., and Strecker, M. R. (2011a). Hillslope-glacier coupling: The interplay of topography and glacial dynamics in High Asia. *Journal of Geophysical Research: Earth Surface*, 116(F2).

Scherler, D., Bookhagen, B., and Strecker, M. R. (2011b). Spatially variable response of Himalayan glaciers to climate change affected by debris cover. *Nature Geoscience*, 4(3):156–159.

Scherler, D., Leprince, S., and Strecker, M. R. (2008). Glacier-surface velocities in alpine terrain from optical satellite imagery-Accuracy improvement and quality assessment. *Remote Sensing of Environment*, 112(10):3806–3819.

Schoof, C. (2005). The effect of cavitation on glacier sliding. *Proceedings of the Royal Society A: Mathematical, Physical and Engineering Sciences*, 461(2055):609–627.

Song, C., Sheng, Y., Wang, J., Ke, L., Madson, A., and Nie, Y. (2017). Heterogeneous glacial lake changes and links of lake expansions to the rapid thinning of adjacent glacier termini in the Himalayas. *Geomorphology*, 280:30–38.

Steiner, J. F., Buri, P., Miles, E. S., Ragettli, S., and Pellicciotti, F. (2019). Supraglacial ice cliffs and ponds on debris-covered glaciers: Spatio-temporal distribution and characteristics. *Journal of Glaciology*, 65(252):617–632.

Stumpf, A., Michéa, D., and Malet, J. P. (2018). Improved co-registration of Sentinel-2 and Landsat-8 imagery for Earth surface motion measurements. *Remote Sensing*, 10(2).

Tadono, T., Ishida, H., Oda, F., Naito, S., Minakawa, K., and Iwamoto, H. (2014). Precise Global DEM Generation by ALOS PRISM. *ISPRS Annals of Photogrammetry, Remote Sensing and Spatial Information Sciences*, II-4:71–76.

The RGI Consortium (2017). Randolph Glacier Inventory – A Dataset of Global Glacier Outlines: Version 6.0, GLIMS Technical Report. Technical Report July.

Truffer, M. (2004). The basal speed of valley glaciers: An inverse approach. *Journal of Glaciology*, 50(169):236–242.

Truffer, M. and Motyka, R. J. (2016). Where glaciers meet water: Subaqueous melt and its relevance to glaciers in various settings.

Tsutaki, S., Fujita, K., Nuimura, T., Sakai, A., Sugiyama, S., Komori, J., and Tshering, P. (2019). Contrasting thinning patterns between lake- And land-terminating glaciers in the Bhutanese Himalaya. *Cryosphere*, 13(10):2733–2750.

Tsutaki, S., Sugiyama, S., Sakakibara, D., and Sawagaki, T. (2016). Surface elevation changes during 2007-13 on Bowdoin and Tugto Glaciers, northwestern Greenland. *Journal of Glaciology*, 62(236):1083–1092.

Vieli, A., Funk, M., and Blatter, H. (2001). Flow dynamics of tidewater glaciers: A numerical modelling approach. *Journal of Glaciology*, 47(159):595–606.

Vincent, C., Wagnon, P., Shea, J. M., Immerzeel, W. W., Kraaijenbrink, P., Shrestha, D., Soruco, A., Arnaud, Y., Brun, F., Berthier, E., and Sherpa, S. F. (2016). Reduced melt on debris-covered glaciers: Investigations from Changri Nup Glacier, Nepal. *Cryosphere*, 10(4):1845–1858.

Viviroli, D., Dürr, H. H., Messerli, B., Meybeck, M., and Weingartner, R. (2007). Mountains of the world, water towers for humanity: Typology, mapping, and global significance. *Water Resources Research*, 43(7).

Wangchuck, S. and Bolch, T. . (2020). Mapping of glacial lakes using Sentinel-1 and Sentinel-2 data and a random forest classifier: strengths and challenges. *Science of Remote Sensing*.

Watson, C. S., Kargel, J. S., Shugar, D. H., Haritashya, U. K., Schiassi, E., and Furfaro, R. (2020). Mass Loss From Calving in Himalayan Proglacial Lakes. *Frontiers in Earth Science*, 7.

Whillans, I. M. and Bindschadler, R. A. (1988). Mass balance of Ice Stream B. West Antarctica. *Annals of Glaciology*, 11:187–193.

Wijngaard, R. R., Steiner, J. F., Kraaijenbrink, P. D., Klug, C., Adhikari, S., Banerjee, A., Pellicciotti, F., van Beek, L. P., Bierkens, M. F., Lutz, A. F., and Immerzeel, W. W. (2019). Modeling the response of the langtang glacier and the hintereisferner to a changing climate since the little ice age. *Frontiers in Earth Science*, 7:143.

Willis, M. J., Melkonian, A. K., Pritchard, M. E., and Ramage, J. M. (2012). Ice loss rates at the Northern Patagonian Icefield derived using a decade of satellite remote sensing. *Remote Sensing of Environment*, 117:184–198.

Zhang, G., Yao, T., Xie, H., Wang, W., and Yang, W. (2015). An inventory of glacial lakes in the Third Pole region and their changes in response to global warming. *Global and Planetary Change*, 131:148–157.

Zhou, Y., Li, Z., Li, J., Zhao, R., and Ding, X. (2018). Glacier mass balance in the Qinghai–Tibet Plateau and its surroundings from the mid-1970s to 2000 based on Hexagon KH-9 and SRTM DEMs. *Remote Sensing of Environment*, 210:96–112.

Appendices

A Additional Materials Velocity Quality Assessment

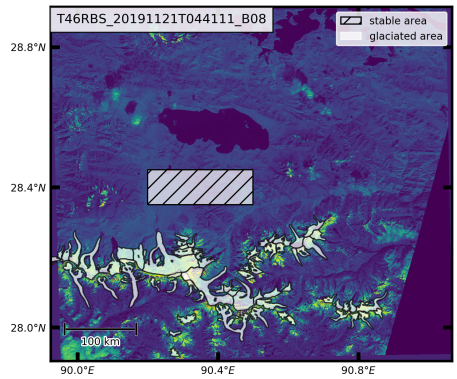

Figure A.1: Sentinel-2 image tile with the selected surface area used for image-matching represented by the white mask.

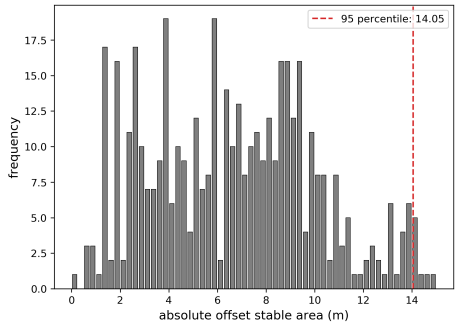

Figure A.2: Distribution of all absolute median offsets calculated at stable areas ($\overline{V}_{off}$). Red dashed line represents the 95% percentile.

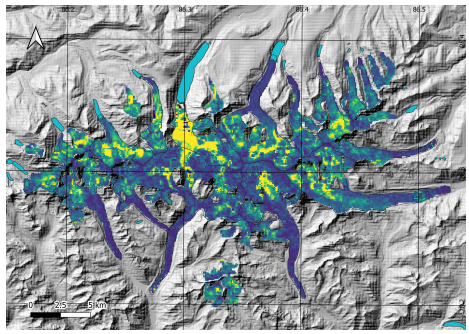

Figure A.3: The MAD_{disp} at subselection at region Central 1. Yellow areas indicate surfaces with MAD_{disp} >10m/year.

Table A.1: Parameters for the linear regression between $\log(\frac{CI_{95}}{MAD_{disp}})$ and log(N).

Satellite area	component	α	k	R^2
T44RPU	x	0.38	3.9	0.87
	y	0.49	5.7	0.92
T44RPT	x	0.45	3.1	0.89
	y	0.50	3.7	0.92
T45RTN	x	0.53	4.0	0.92
	y	0.54	4.2	0.94
T45RTM	x	0.48	4.8	0.92
	y	0.51	5.0	0.93
T45RUM	x	0.35	3.4	0.88
	y	0.40	3.8	0.89
T45RVM	x	0.36	3.9	0.90
	y	0.41	4.2	0.91
T45RVL	x	0.58	5.8	0.94
	y	0.62	5.3	0.96
T45RWL	x	0.66	5.5	0.97
	y	0.67	6.0	0.93
T45RXL	x	0.69	6.2	0.92
	y	0.64	5.9	0.95
T45RYM	x	0.34	3.6	0.88
	y	0.38	5.3	0.92
T46RBS	x	0.34	3.6	0.88
	y	0.37	3.8	0.93

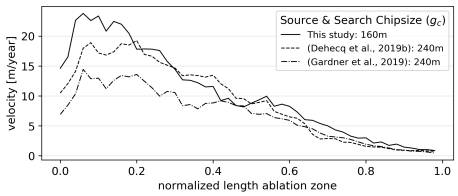

Figure A.4: Regional median centre flow line surface velocity (m/year) comparison between Dehecq et al. (2019b) (dashed line), Gardner et al. (2019) (dashed-dotted line) and this study (solid line) of glacier greater than 10km^2 in area.

B Additional Materials Centre Flow Line Analysis

Table B.1: Mean of median centre flow line velocities and slope of lake-terminating and land-terminating glaciers in m/year for second half of the ablation zone. Uncertainty estimates represent the 1 SE confidence interval.

	Terminus Type		
Glacier Features	Lake	Land	All
Slope (degrees)	-7.2 ±3.7	-8.2 ±4.54	-8.0 ±4.2
Velocity (m/year)	17.7 ±0.47	3.9 ±0.09	5.2 ±0.11

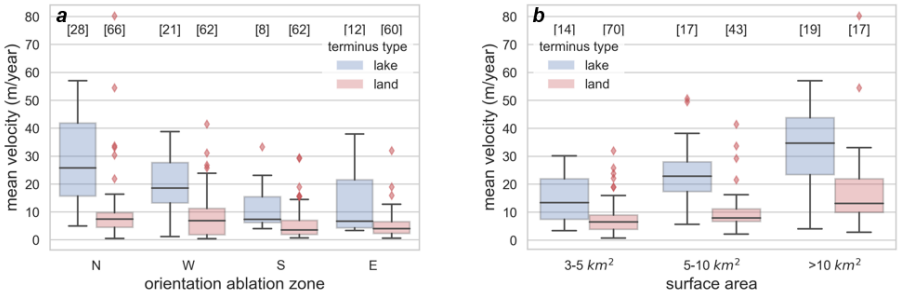

Figure B.1: Boxplot showing the mean velocity contrast between lake-terminating glaciers (blue) and land-terminating glaciers (red) depending on the orientation of the ablation zone (a) and surface area (b) for the second half of the ablation zone. Boxes represent the IQR of the distribution, whereas points that are outside of the 3rd quartile plus 1.5 times the IQR range are plotted explicitly.

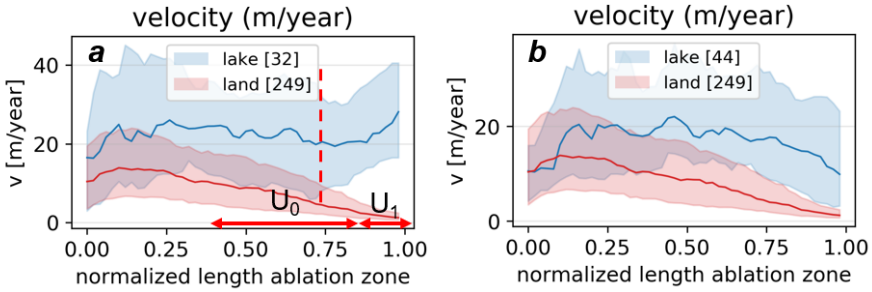

Figure B.2: A rough separation of accelerating (a) and deceleration (b) lake-terminating glaciers. A glacier is regarded as accelerating when the mean velocity U_1 is greater than mean velocity U_0. Red dashed line is the estimated location where the acceleration becomes observable. Land-terminating glaciers are plotted for reference.